AGU PUBLICATIONS

JGR

Journal of Geophysical Research: Solid Earth

RESEARCH ARTICLE

10.1002/2014JB011612

Key Points:
- Generalization of the critical Coulomb wedge (CCW) theory by limit analysis
- Constrain mechanical properties and overpressures in North Chile
- Provide the exact CCW solution in two appendices

Supporting Information:
- Text S1

Correspondence to:
X. P. Yuan,
xyuan@geologie.ens.fr

Citation:
Yuan, X. P., Y. M. Leroy, and B. Maillot (2015), Tectonic and gravity extensional collapses in overpressured cohesive and frictional wedges, *J. Geophys. Res. Solid Earth*, *120*, doi:10.1002/2014JB011612.

Received 18 SEP 2014
Accepted 13 JAN 2015
Accepted article online 18 JAN 2015

Tectonic and gravity extensional collapses in overpressured cohesive and frictional wedges

X. P. Yuan[1], Y. M. Leroy[1,2], and B. Maillot[3]

[1]Laboratoire de Géologie, UMR 8538, CNRS, École Normale Supérieure, Paris, France, [2]Now at Total, CSTJF, Pau, France, [3]Laboratoire GEC, Université de Cergy-Pontoise, Cergy-Pontoise, France

Abstract Two modes of extensional collapse in a cohesive and frictional wedge of arbitrary topography, finite extent, and resting on an inclined weak décollement are examined by analytical means. The first mode consists of the gravitational collapse by the action of a half-graben, rooting on the décollement and pushing seaward the frontal part of the wedge. The second mode results from the tectonics extension at the back wall with a similar half-graben kinematics and the landward sliding of the rear part of the wedge. The predictions of the maximum strength theorem, equivalent to the kinematic approach of limit analysis and based on these two collapse mechanisms, not only match exactly the solutions of the critical Coulomb wedge theory, once properly amended, but generalizes them in several aspects: wedge of finite size, composed of cohesive material and of arbitrary topography. This generalization is advantageous to progress in our understanding of many laboratory experiments and field cases. For example, it is claimed from analytical results validated by experiments that the stability transition for a cohesive, triangular wedge occurs with the activation of the maximum length of the décollement. It is shown that the details of the topography, for the particular example of the Mejillones peninsula (North Chile) is, however, responsible for the selection of a short length-scale, dynamic instability corresponding to a frontal gravitational instability. A reasonable amount of cohesion is sufficient for the pressures proposed in the literature to correspond to a stability transition and not with a dynamically unstable state.

1. Introduction

The kinematic approach of limit analysis, also called the maximum strength theorem (MST) [*Maillot and Leroy*, 2006] for compressional deformation in fluid-saturated porous media [*Pons and Leroy*, 2012], is extended to the extensional context. The objective of this work is to propose this simple method to analyze the gravity and tectonic extensional deformation modes occurring in overpressured frictional wedges extending the stability conditions presented by *Dahlen* [1984] and *Xiao et al.* [1991] to arbitrary-shaped topography and cohesive materials.

Two kinds of collapse modes, combinations of normal faults and axial surfaces, typical of tectonics areas in extension are considered. For example, the Schell Creek range, Nevada, presents a collapse mechanism composed of a normal fault and an axial surface, both rooting on a weak décollement. This asymmetric collapse mode is referred to as a half-graben [*Groshong*, 1989]. It is a mechanical instability that typically results from excessive sedimentation and/or weakening of a detachment horizon as seen in river deltas [*Mandl and Crans*, 1981] or in the shallow portion of the convergent margin off Antofagasta [*Delouis et al.*, 1998; *von Huene and Ranero*, 2003; *Sallarès and Ranero*, 2005]. This gravitational collapse is the first mechanism to be studied in this contribution in the context of fluid-saturated wedges. The second mode of instability is due to a regional extensional tectonic event (e.g., Brazos Ridge fault, offshore Texas [*Xiao et al.*, 1991; *Withjack et al.*, 1995]). This second mode which is also based on the half-graben kinematics described above is referred to as a tectonic extensional collapse.

Sandbox analogue experiments have been proposed to validate the field interpretation either at the subduction scale [*Xiao and Suppe*, 1992] or on the length scale of the half-graben which could structure a hydrocarbon reservoir [*Patton*, 2005]. Recently, an impressive effort has been conducted to create analogue experiments with fluid overpressure by controlling the air flow through the base [*Mourgues and Cobbold*, 2003; *Mourgues et al.*, 2009; *Lacoste et al.*, 2012]. Such developments bring us one step closer to the conditions found in sedimentary basins and accretionary wedges. They call for new theoretical

developments to capture the onset and the evolution of failure in overpressured materials. This is an important motivation for the present work.

Most of our theoretical understanding is based on the critical Coulomb wedge (CCW) theory [*Davis et al.*, 1983] first proposed for compressional wedges. *Dahlen* [1984] introduces extensional conditions which are pertinent to our gravitational collapse mode. The work of *Xiao et al.* [1991] further generalizes the CCW theory by reversing the sense of slip on the décollement which corresponds to our tectonic collapse mode. The solution in the last two references is nevertheless approximate in the sense that its validity is limited to low topographic slopes and pore pressures. It is only recently that the CCW theory was amended by *Wang et al.* [2006] to produce an exact solution (called the exact critical Coulomb wedge (ECCW) theory in this contribution) that was applied to sandbox experiments [*Mourgues et al.*, 2014].

This contribution contents are as follows: Next section is concerned with the general stability conditions for a wedge of arbitrary topography and composed of a cohesive, frictional material. The stability conditions are specialized in section 3 for our gravitational instability mode. The special case of a triangular wedge composed of a cohesionless material is then proposed preparing the grounds for the successful comparison with the ECCW theory. The two challenges of this comparison are first to make sure that our parametrization of the pressure ratio is identical to the one proposed by *Dahlen* [1984] (see Appendix A) and second to complement the modification proposed by *Wang et al.* [2006] to obtain the exact implicit solution (ECCW) (see Appendix B). For the case of cohesive materials and a triangular wedge, it is found that the stability transition is associated with the gravitational collapse along the maximum possible décollement length. This claim is validated by comparing our predictions with the results of a series of experiments with sand and plaster, the proportion of the later material controlling the overall cohesion. Section 4 sees the application of the general stability conditions to tectonic collapse. The comparison with the ECCW theory is then presented before the MST is applied to the sandbox experiments of *Xiao et al.* [1991]. It is shown that our approach not only captures the onset of collapse but also predicts the evolution of the deformation style during the retreat of the vertical wall. To show the versatility of our method, section 5 is proposed to analyze the stability conditions of the active margin off Antofagasta in North Chile [*von Huene and Ranero*, 2003; *Sallarès and Ranero*, 2005]. It is shown that the pressure conditions proposed in *von Huene and Ranero* [2003] imply a dynamically unstable state, unless some bulk cohesion is introduced. At 5 MPa bulk cohesion, the wedge is in a stable mode, very near quasi-static instability. This stability transition is consistent with the quasi-static topographic evolution responsible for the debris flow toward the subduction channel [*Delouis et al.*, 1998].

2. Limit Analysis for Extension

The objective of this section is to present the theory used throughout this contribution and, in particular, to define the concept of collapse mechanism.

2.1. Prototype and Collapse Mechanisms

The geometry of our prototype and of the collapse mechanism is presented in Figure 1. It consists of a wedge of arbitrary topography and of a triangular-like shape resting on a straight décollement (*AB*) inclined at an angle β (positive if dipping landward as in Figure 1b; $\bar{\beta}$ is the absolute value of β). The two collapse mechanisms in Figures 1a and 1b consist of a normal fault bounding a half-graben (HG). Material within the HG is sliding on the normal fault (solid segments, *JH* and *GE* dipping at γ), and part of this material is crossing the conjugate shear plane (dotted segments, *JI* and *GF*, dipping at θ). This material flux results in the push of the frontal section (labeled FS for frontal and seaward) or of the back region (labeled BL for back and landward), as in Figures 1a and 1b, respectively. In the former case, the collapse is purely gravitational, and in the latter case it is due to the retreat of the back wall (*AC*), boundary of the wedge and the collided plate, because of a tectonic extension. Note that in Figure 1b, the large arrow indicates the sense of compression. In the tectonic extension case, the force Q_e will often be compressive, but not necessarily.

The rest of this section presents the theory necessary to decide on the position of the collapse mechanism (points *G* or *J*) and the dip of the normal fault and the shear plane. The position of the three points *EFG* or *HIJ* define entirely the collapse mechanism referred to as the gravitational (Figure 1a) and the tectonic mode (Figure 1b), respectively.

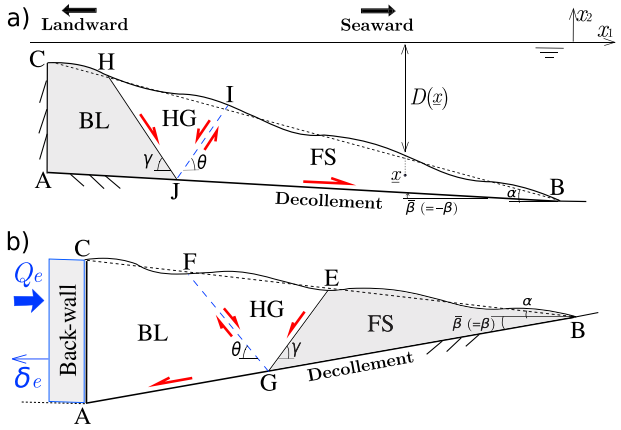

Figure 1. Definition of the two collapse modes: (a) the gravity collapse mode relies on a half-graben (HG) with seaward slip of the frontal section (labeled FS for front and seaward) on the décollement; (b) the tectonic collapse mode has a similar kinematics with slip of the back region (labeled BL for back and landward) associated to the landward slip of the HG along the normal fault *GE*. The distance $D(\underline{x})$ defines the depth of the submerged domain over any material point located by the vector $\underline{x}$.

2.2. Theorem of Effective Virtual Powers

This theorem is the weak form (integral) of the equation of motion and was presented in *Pons and Leroy* [2012] except for the introduction of inertia:

$$\mathcal{P}'_{\text{ext}}(\hat{\underline{U}}) - \mathcal{P}'_{\text{int}}(\hat{\underline{U}}) = \mathcal{P}_{\text{acc}}(\hat{\underline{U}}) \quad \forall \quad \hat{\underline{U}}\ KA\,. \tag{1}$$

This theorem is constructed in the supporting information for the sake of completeness. It states the equality between the acceleration power and the difference between the effective external and internal powers for any kinematically admissible (KA) velocity field denoted $\hat{\underline{U}}$. The set of KA fields does not contain just the exact, unknown velocity field but comprises any field consistent with the boundary conditions of our problem. It includes also the piecewise uniform velocity fields $\hat{\underline{U}}$ associated to the kinematics of the two collapse mechanisms described above.

The effective external power is defined by

$$\mathcal{P}'_{\text{ext}}(\hat{\underline{U}}) = \int_{\partial\Omega_t^T} \underline{T}^d \cdot \hat{\underline{U}}\,\mathrm{d}S + \int_{\Omega_t} \rho\underline{g} \cdot \hat{\underline{U}}\,\mathrm{d}V + \int_{\Omega_t} p\,\mathrm{div}\hat{\underline{U}}\,\mathrm{d}V + \int_{\Sigma_U} p_\Sigma \underline{n} \cdot \hat{\underline{J}}\,\mathrm{d}S\,. \tag{2}$$

The first term is the force per unit area $\underline{T}^d$ applied on $\partial\Omega_t^T$, part of the wedge boundary (for example, the sea fluid pressure over the topography *BC*). The second term is the power of the gravity field (ρ is the fluid-saturated volumetric mass and $\underline{g}$ the gravity acceleration vector) in the domain occupied by the wedge (Ω_t) (Figure 1). The last two terms in (2) correspond to the power of the velocity field $\hat{\underline{U}}$ on the fluid pressure, seen as an external field, either in the bulk or within any velocity discontinuity ($\hat{\underline{J}}$) along a surface of normal $\underline{n}$. These velocity discontinuities are found across the normal fault, the shear plane, the activated part of the décollement and possibly at the contact with the back wall. All these surfaces are grouped in the set Σ_U. Note in (2) that the pressure p in the bulk could be different from the pressure p_Σ found in the discontinuities. No attempt is made to justify the origins and how such pressure discontinuities are maintained in time.

The effective internal power introduced in (1) reads

$$\mathcal{P}'_{\text{int}}(\hat{\underline{U}}) = \int_{\Omega_t} \underline{\underline{\sigma}}' : \hat{\underline{\underline{d}}}\,\mathrm{d}V + \int_{\Sigma_U} \underline{T}'_\Sigma \cdot \hat{\underline{J}}\,\mathrm{d}S\,, \tag{3}$$

and corresponds to the effective stress tensor $\underline{\underline{\sigma}}'$ multiplied by the rate of deformation tensor $\hat{\underline{\underline{d}}}$ (computed from the virtual velocity field $\hat{\underline{U}}$) and to the effective stress vector $\underline{T}'_\Sigma$ times the velocity jump across the surfaces in the set Σ_U. All the velocity fields considered herein will be piecewise continuous so that only discontinuities will contribute to the effective internal power.

The acceleration power in (1) is

$$\mathcal{P}_{\text{acc}}(\hat{\underline{U}}) = \int_{\Omega_t} \rho\underline{a} \cdot \hat{\underline{U}}\,\mathrm{d}V\,, \tag{4}$$

with $\underline{a}$ denoting the acceleration field. Note that the sign of this power depends on the orientation of the velocity field with respect to the acceleration.

To complement these definitions, we need to introduce the effective stress carried by the solid phase of our fluid-saturated continuum

$$\underline{\underline{\sigma}}' = \underline{\underline{\sigma}} + p\underline{\underline{\delta}}\,, \tag{5}$$

where $\underline{\underline{\delta}}$ is the identity tensor, as well as the effective stress vector on any surface

$$\underline{T}' = \underline{T} + p\underline{n}\,, \tag{6}$$

oriented by its normal $\underline{n}$.

The last ingredient required to complete this section is the parametrization of the pressure field. The proposition of *Hubbert and Rubey* [1959] is adopted here with the following fluid pressure ratio:

$$\lambda(\underline{x}) = -\frac{p(\underline{x}) - \rho_f g D(\underline{x})}{\sigma(\underline{x}) + \rho_f g D(\underline{x})} \quad \text{with} \quad \sigma(\underline{x}) = \rho g(x_2 + D(\underline{x})) - \rho_f g D(\underline{x})\,, \tag{7}$$

in which ρ_f and $D(\underline{x})$ are the fluid volumetric mass and the thickness of the fluid above the saturated continuum at point $\underline{x}$ (see Figure 1a for illustration), respectively. The stress σ in (7) is negative and corresponds to the pressure resulting from the weight of the column above the point $\underline{x}$ of interest. The second axis is vertical and directed upward, Figure 1a, so that the gravity acceleration vector is $\underline{g} = -g\underline{e}_2$. The scalar λ in (7) varies between ρ_f/ρ and 1 corresponding to the range of pressure between hydrostatic and lithostatic. The fluid pressure ratio λ can also be expressed as the sum of the overpressure ratio difference $\Delta\lambda$ and the hydrostatic pressure ratio λ_{hydro}

$$\lambda = \Delta\lambda + \lambda_{\text{hydro}} \quad \text{with} \quad \lambda_{\text{hydro}} = \rho_f/\rho, \tag{8}$$

so that $\Delta\lambda$ varies within the range of 0 and $1 - \rho_f/\rho$. The fluid pressure p and its difference from the hydrostatic pressure at any point of the medium are thus expressed as

$$p = g[-\lambda\rho x_2 + (\rho_f - \rho\lambda)D] \quad \text{and} \quad \Delta p = -\Delta\lambda\rho g(x_2 + D)\,. \tag{9}$$

Note that the fluid pressure parametrization relies on the vertical axis of our coordinate system and not on the distance to the topography. This difference is crucial to understand some of the discrepancies found in the application of the CCW theory and discussed in what follows.

2.3. MST

A weak form of the equations of motion has just been introduced. The effective internal and the acceleration powers for our examples are nevertheless unknown since neither the stress vector acting on the discontinuities nor the acceleration are determined. The application of the maximum strength theorem (MST) palliates to this difficulty and provides the dominant collapse mechanism, a concept to be defined, after a few assumptions on the material strength are discussed. Before proceeding, the reader should be warned that there is still a strong debate in the mechanics literature on the validity of this MST [see *Chen*, 1975 and *Michalowski*, 1995, for references] because of the interpretation of the virtual velocity. We favor the school of thoughts relying on convex analysis [*Salençon*, 2002] and discussed at length in *Maillot and Leroy* [2006] and *Souloumiac et al.* [2010]. Comparison with an exact solution (ECCW) as well as experimental results are hoped to justify our preference.

The effective stress vector acting on a discontinuity of normal $\underline{n}$ and tangent $\underline{t}$, member of Σ_U, is decomposed in a normal σ'_n and a tangential component τ in the right-handed basis $\{\underline{n}, \underline{t}\}$. This vector is within the set

$$G = \{\underline{T}' \,|\, |\tau| + \tan(\varphi)\sigma'_n - C \leq 0\}\,, \tag{10}$$

bounded by the Coulomb criterion defined by the friction angle φ and the cohesion C. This set is convex in the space (τ, σ'_n), an essential property for what follows. Consider now the jump in velocity across any discontinuity $\hat{\underline{J}}$ where the effective stress vector $\underline{T}'$ is acting and apply convex analysis [*Salençon*, 2002] to see that there is a maximum to the power $\underline{T}' \cdot \hat{\underline{J}}$ which is called the support function $\pi(\hat{\underline{J}})$. This function depends on the orientation η of $\hat{\underline{J}}$, the angle, counted positive anticlockwise, with the normal to the plane of discontinuity ($\hat{\underline{J}} \cdot \underline{n} = \hat{J}\cos\eta$). The experience of previous works with this theoretical framework without pressure

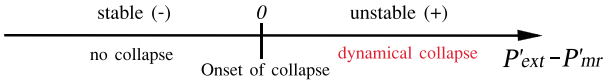

Figure 2. The stability conditions are defined along the axis set by the difference $\mathcal{P}'_{\text{ext}} - \mathcal{P}'_{\text{mr}}$.

field [*Cubas et al.*, 2008] or including the fluid phase [*Pons and Leroy*, 2012] is that the velocity jumps have to be selected such that $\eta = \pm(\pi/2 - \varphi)$. These special orientations correspond to the minimum value of the support function, which is then expressed as

$$\pi(\underline{\hat{J}}) = \hat{J}C\cos\varphi, \quad \text{with } \underline{\hat{J}} \cdot \underline{n} = \hat{J}\cos\eta \quad \text{and} \quad \eta = \pm(\pi/2 - \varphi). \tag{11}$$

The support function is integrated along the discontinuities constituting the set Σ_U to provide the maximum resisting power

$$\mathcal{P}'_{\text{mr}}(\underline{\hat{U}}) = \int_{\Sigma_U} \pi(\underline{\hat{J}})\,\mathrm{d}S \geq \mathcal{P}'_{\text{int}}(\underline{\hat{U}}), \tag{12}$$

which is bounding by above the unknown effective internal power. Combined with the theorem of effective virtual powers in (1), this bounding provides

$$\mathcal{P}'_{\text{ext}}(\underline{\hat{U}}) - \mathcal{P}_{\text{acc}}(\underline{\hat{U}}) \leq \mathcal{P}'_{\text{mr}}(\underline{\hat{U}}) \quad \forall \quad \underline{\hat{U}}\,KA. \tag{13}$$

If the effective external power is smaller than the maximum resisting power for any KA velocity field, the structure is said to be stable under quasi-static conditions (no inertia). It is the condition $\mathcal{P}'_{\text{ext}} = \mathcal{P}'_{\text{mr}}$ for a given velocity field which signals the quasi-static onset of collapse. If the difference $\mathcal{P}'_{\text{ext}} - \mathcal{P}'_{\text{mr}}$ is positive, the structure is said to be dynamically unstable. The collapse mechanism corresponding to the maximum value of that difference is said to be dominant and does control the stability conditions, illustrated in Figure 2.

3. Gravitational Collapse

The MST is now applied to the gravitational collapse mode to obtain general stability conditions. These conditions are then specialized to the particular case of cohesionless materials and of a triangular-shaped wedge so that the comparison with the classical CCW theory is possible. The role of the length-scale set by the cohesion in the stability conditions is then discussed before presenting laboratory experiments to validate the proposed theory.

3.1. General Stability Conditions Based on the MST

The KA velocity field for gravitational collapse is piecewise uniform. It is different over the frontal region (FS), the half-graben (HG), and the back region (BL), Figure 3a. The support function in (11) guides us in orienting the velocity in each region: the velocity of the FS is inclined by the angle φ_D from the décollement and has for norm $\hat{U}_{\text{FS}}$. The HG velocity is inclined by the angle φ_{NF} from the normal fault *JH* and has the norm $\hat{U}_{\text{HG}}$. The BL has a null velocity since the back wall is not displaced. The velocity jump at the shear plane *JI* is the difference $\underline{\hat{U}}_{\text{FS}} - \underline{\hat{U}}_{\text{HG}}$, a vector of norm $\hat{J}_{\text{SP}}$ and oriented by the angle φ_{SP} from *JI* in Figure 3a. The velocity vectors are thus all oriented, and we are left with the determination of their norms. The hodograph of the velocity jump across the shear plane which is presented in Figure 3b provides that information by application of the law of the sines

$$\frac{\hat{U}_{\text{HG}}}{\sin(\theta - \varphi_{\text{SP}} - \beta - \varphi_D)} = \frac{\hat{U}_{\text{FS}}}{\sin(\theta + \gamma - \varphi_{\text{SP}} - \varphi_{\text{NF}})} = \frac{\hat{J}_{\text{SP}}}{\sin(\gamma + \beta - \varphi_{\text{NF}} + \varphi_D)}. \tag{14}$$

There is nevertheless an indeterminacy in the value of the three ratios in (14) which is eliminated by setting one of them arbitrarily equal to 1.

The external effective power defined in (2) for this velocity field reads

$$\begin{aligned}\mathcal{P}'_{\text{ext}}(\underline{\hat{U}}) = \rho\underline{g} \cdot (S_{\text{FS}}\underline{\hat{U}}_{\text{FS}} + S_{\text{HG}}\underline{\hat{U}}_{\text{HG}}) + \int_J^B p_D\,\mathrm{d}S\,\underline{n}_{JB} \cdot \underline{\hat{U}}_{\text{FS}} + \int_J^I p_{JI}\,\mathrm{d}S\,\underline{n}_{JI} \cdot \underline{\hat{J}}_{\text{SP}} \\ + \int_J^H p_{JH}\,\mathrm{d}S\,\underline{n}_{JH} \cdot \underline{\hat{U}}_{\text{HG}} + \int_H^I p\,\mathrm{d}S\,\underline{n}_{HI} \cdot \underline{\hat{U}}_{\text{HG}} + \int_I^B p\,\mathrm{d}S\,\underline{n}_{IB} \cdot \underline{\hat{U}}_{\text{FS}},\end{aligned} \tag{15}$$

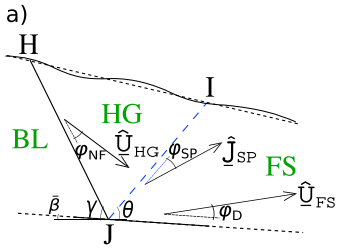

Figure 3. (a) The velocity field for the gravitational collapse. (b) The hodograph of the velocity jump across the shear plane *JI*.

in which S_{FS} and S_{HG} are the areas of the front and the half-graben, respectively. The first term in the right-hand side of (15) corresponds to the power of the velocity field on gravity. The next three integrals are the contributions of the power of the velocity on the pressure field within the décollement (*JB*), the shear plane (*JI*), and the normal fault (*JH*), respectively. The last two terms result from the power of the pressure on the topography. Note that the velocity field being divergence free, there is no contribution to the effective external power of the pressure field within the bulk. Expression (15) is now simplified by application of the following weak form of Archimedes' theorem (see derivation in the supporting information): the power of the velocity field on the hydrostatic part of the pressure is equal to the opposite of the power of the same velocity field on the vertical forces resulting from the weight of the displaced regions, if assumed of density ρ_f. The effective external power is then

$$\begin{aligned}\mathcal{P}'_{\text{ext}}(\hat{\underline{U}}) = (\rho-\rho_f)\underline{g}\cdot\left(S_{FS}\hat{\underline{U}}_{FS}+S_{HG}\hat{\underline{U}}_{HG}\right)\\ +\int_J^B \Delta p_D\,\mathrm{d}S\,\underline{n}_{JB}\cdot\hat{\underline{U}}_{FS}+\int_J^I \Delta p_{JI}\,\mathrm{d}S\,\underline{n}_{JI}\cdot\hat{\underline{J}}_{SP}+\int_J^H \Delta p_{JH}\,\mathrm{d}S\,\underline{n}_{JH}\cdot\hat{\underline{U}}_{HG}\,,\end{aligned} \tag{16}$$

and is expressed simply in terms of the departure of the pressure from the hydrostatic condition.

The maximum resisting power in (12) is now combined with the support function in (11) for the proposed velocity field:

$$\mathcal{P}'_{\text{mr}}(\hat{\underline{U}}) = C_D L_{JB}\cos(\varphi_D)\hat{U}_{FS}+C_{NF}L_{JH}\cos(\varphi_{NF})\hat{U}_{HG}+C_{SP}L_{JI}\cos(\varphi_{SP})\hat{J}_{SP}\,. \tag{17}$$

It is the sum of the contribution of the décollement segment *JB*, the normal fault *JH* and of the shear plane *JI*.

Application of the MST requires now to maximize the difference $\mathcal{P}'_{\text{ext}}-\mathcal{P}'_{\text{mr}}$ in terms of the dips γ and θ and the length L_{JB}. If that maximum is negative, the system is stable, otherwise there is a quasi-static or a dynamic instability and the optimum triplet of parameters (γ, θ, and L_{JB}) define the dominant collapse mechanism.

3.2. Comparison With CCW Theory

The general solution in (16) and (17) is now specialized for the case of cohesionless materials. The maximum resisting power is then null and the stability condition reduces to $\mathcal{P}'_{\text{ext}}=0$. In this instance, and for a triangular wedge, the effective external power (16) reduces to

$$\begin{aligned}\mathcal{P}'_{\text{ext}}(\hat{\underline{U}}) = (\rho-\rho_f)g\left[S_{HG}\hat{U}_{HG}\sin(\gamma-\varphi_{NF})-S_{FS}\hat{U}_{FS}\sin(\varphi_D+\beta)\right]\\ +\Delta\lambda_B\rho g\frac{L_{JH}^2\sin(\gamma-\alpha)}{2\cos\alpha}\hat{U}_{HG}\sin(\varphi_{NF})+\Delta\lambda_B\rho g\frac{L_{JI}^2\sin(\theta+\alpha)}{2\cos\alpha}\hat{J}_{SP}\sin(\varphi_{SP})\\ +\Delta\lambda_D\rho g\frac{L_{JB}^2\sin(\alpha+\beta)}{2\cos\alpha}\hat{U}_{FS}\sin(\varphi_D)=0\end{aligned}$$

with

$$\begin{aligned}S_{HG}=\frac{\sin^2(\alpha+\beta)\sin(\gamma+\theta)}{2\sin(\gamma-\alpha)\sin(\theta+\alpha)}L_{JB}^2\,,\quad S_{FS}=\frac{\sin(\alpha+\beta)\sin(\theta-\beta)}{2\sin(\theta+\alpha)}L_{JB}^2\,,\\ L_{JH}=\frac{\sin(\alpha+\beta)}{\sin(\gamma-\alpha)}L_{JB}\quad\text{and}\quad L_{JI}=\frac{\sin(\alpha+\beta)}{\sin(\theta+\alpha)}L_{JB}\,,\end{aligned} \tag{18}$$

in which $\Delta\lambda_B$ and $\Delta\lambda_D$ are the fluid overpressure ratios of the bulk material and the décollement, respectively. In accordance with the assumption of the CCW theory, the fluid ratios and friction angles in the normal fault *JH* and shear plane *JI* are set to the bulk ratio $\Delta\lambda_B$ and the bulk friction angle φ_B.

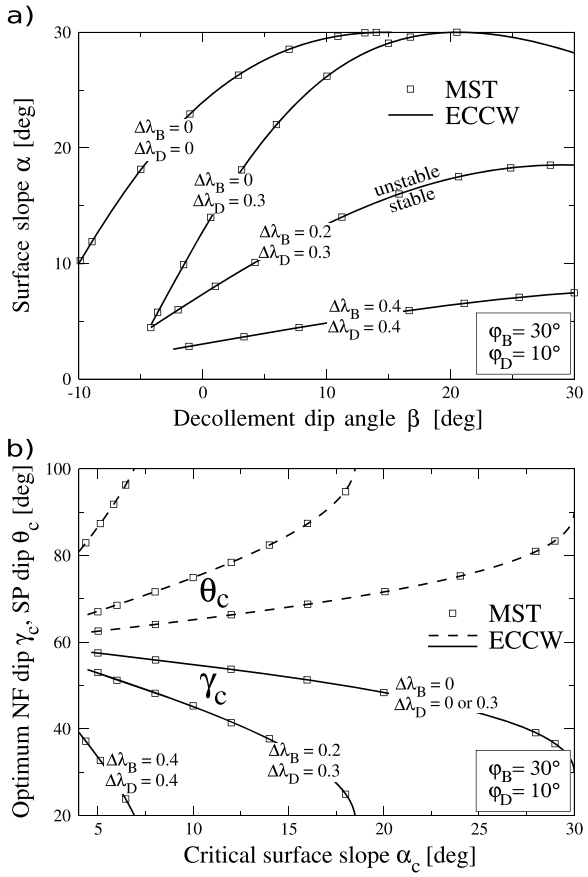

Figure 4. (a) Comparison of MST (symbols) and ECCW predictions (curves) for cohesionless materials, overpressure ratio $\Delta\lambda_D$ in the décollement and bulk fluid overpressure ratio $\Delta\lambda_B$. (b) The optimum dips of the normal fault (NF, γ_c) and of the shear plane (SP, θ_c) determined by the ECCW (solid and dashed curves, respectively) and by the MST (symbols).

It is necessary to maximize (18) with respect to the two angles θ and γ. Stability requires this function to be negative at its maximum. Note from (18) that the external power is proportional to the square of the length L_{JB} of the structure. As a consequence, this length is not an outcome of the optimization and remains arbitrary. This indeterminacy is a common feature with the CCW theory. Furthermore, the slope α can be varied in the MST approach as a parameter to find the critical value α_c for which there is a transition from stable to unstable conditions. In that sense, it is intended to prove next that the results of the optimization and the parametric study are identical to those of the CCW theory.

The comparison of the MST and CCW predictions requires to use identical definition of the overpressure ratios and thus of the distance z to the sea floor. This z axis is vertical in the original work of *Hubbert and Rubey* [1959] as well as in *Pons and Leroy* [2012] and in the present contribution. The z axis is perpendicular to the décollement in *Davis et al.* [1983] and to the topography in *Dahlen* [1984] and *Lehner* [1986]. This last choice is certainly in line with the classic Rankine assumption that stress varies with distance to the topography and not with the position along it. However, it leads to differences in the pressure ratio definition compared to the original definition adopted herein. The differences are presented in details in Appendix A.

There is a further complexity in the comparison of the MST and the CCW predictions due to an approximation introduced by *Dahlen* [1984]. He assumed that the normal stress to the décollement can be approximated by the stress normal to the topography, and he obtained an effective friction coefficient in the décollement. The result of this approximation is a simple, albeit implicit expression for the critical taper angle which is widely used today. The approximation is acceptable in compression since the taper angle is small but leads to a loss of accuracy in extensional regime for which the taper angle is worth several tens of degrees. This shortcoming was recognized and corrected by *Wang et al.* [2006]. This modification of the original work of *Dahlen* [1984] is referred to in what follows as the exact critical Coulomb wedge (ECCW) theory and is presented in Appendix B to complement the presentation of *Wang et al.* [2006].

Comparison of the MST and ECCW predictions are presented in Figure 4, the properties corresponding to the third column of the Table 1. The MST predictions are obtained as follows: choose a value of β, determine the optimum orientation of the two dips (θ and γ), and check the sign of (18). For example, for $\beta = 20°$ and $\Delta\lambda_B = 0.2, \Delta\lambda_D = 0.3$, the function is negative for α less than 17.3°, approximately, and is positive for larger values. The stability transition α_c is thus determined. The critical slope α_c is presented in Figure 4a as a function of the décollement dip β. The ECCW and the MST results correspond to the solid curves and to the symbols, respectively. The two sets of predictions are identical for the four sets of overpressures in the bulk $\Delta\lambda_B$ and décollement $\Delta\lambda_D$. The range in β does not exceed the bulk frictional angle since gravitational collapse mode not using the décollement is expected beyond this value: the maximum α_c is indeed φ_B, seen as the repose angle. Looking at the various sets of pressure considered in this analysis, note that increasing

Table 1. Geometrical and Material Parameters and Fluid Ratios for the Wedge Analysis[a]

Notation	Definition	Value/Range (Gravitational Collapse)	Value/Range (Tectonic Collapse)	Value/Range (Field Example)	Unit
α	topographic slope	−30–45	−39–39	0–5	deg
β	décollement angle	−10–90	27–90	3.72	deg
L_{AB}	décollement length	-	-	29.1	km
D_C	depth of the back top (point C)	-	-	3.15	km
φ_a	friction angle ($a = B$, SP, NF)	30	39	27.9	deg
φ_D	décollement friction angle	10	27	10, 15	deg
φ_{BW}	back-wall friction angle	-	0–39	-	deg
C_a	cohesion ($a = B$, SP, NF)	$0–0.07\rho g L_{AB}$	0	$(0–10) \times 10^6$	Pa
C_D	décollement cohesion	0	0	0	Pa
C_{BW}	back-wall cohesion	-	0	-	Pa
ρ_f	fluid phase density	1000	1000	1030	kg/m^3
ρ	saturated rock density	2120	2000	2400	kg/m^3
λ_{hydro}	hydrostatic pressure ratio	0.47	0.5	0.42	-
$\Delta\lambda_B$	bulk overpressure ratio	0–0.4	0–0.5	0–0.58	-
$\Delta\lambda_D$	décollement overpressure ratio	0–0.53	0–0.5	0–0.58	-
g	gravity acceleration	9.81	9.81	9.81	m/s^2

[a]Parameters are for the gravitational collapse (third column), the tectonic collapse (fourth column), and for the field study (fifth column). Values are constant or varied within the ranges presented. Notation: B: Bulk, SP: shear plane, NF: normal fault, D: décollement, and BW: back wall.

the bulk and décollement pressure ratios decreases the critical slope α_c. Note also that the gravitational instability mode does not require a seaward dipping décollement (β negative). The pressure and frictional properties of the décollement can overcome the difficulty of pushing upslope the sediments in the frontal section during a gravitational collapse. Finally, note that the two theories do predict the same fault dips θ and γ, Figure 4b.

3.3. The Role of Cohesion in a Triangular Wedge

The CCW theory relies on the assumption of cohesionless materials so that the stress state within the wedge scales with the distance z to the topography. The introduction of cohesion ruins this simplicity and the elegance of a potentially analytical solution for the critical stability conditions. The MST approach does not suffer from such limitations.

The characteristic length is chosen as the extent of the décollement L_{AB}, and this leads to the characteristic stress $\rho g L_{AB}$ taken as the reference stress. Dimensionless quantities are noted with a superposed tilde. The stability criterion (13) with no inertia is written in a dimensionless form, symbolically, as

$$\tilde{L}_{JB}\tilde{\mathcal{P}}'_{ext}(\theta,\gamma) \le \tilde{C}\,\tilde{\mathcal{P}}'_{mr}(\theta,\gamma)\,, \tag{19}$$

where $\tilde{C} = C/(\rho g L_{AB})$ and using expressions (17) and (18). The right-hand side is independent of $\tilde{L}_{JB}$, and the left-hand side is proportional to it. As a consequence, the stability condition (equality in 19) must be true for any admissible value of $\tilde{L}_{JB}$, in particular with its maximum value. Therefore, the stability transition is associated with the maximum value $\tilde{L}_{JB}$, which is close to one for our collapse mechanism.

The influence of the bulk cohesion on the critical slope α_c is now presented in Figure 5a where the activation of the whole décollement is assumed ($\tilde{L}_{JB} = 1$, for sake of simplicity). The physical properties are given in the third column of Table 1. The dimensional décollement cohesion $\tilde{C}_D$ is set to zero, the bulk cohesion $\tilde{C}_B$ is varied from 0 to 0.07, and the décollement dip β is set to zero. Results are obtained for dry conditions (blue curve), hydrostatic conditions ($\Delta\lambda_B = \Delta\lambda_D = 0$, black curve), décollement overpressure conditions ($\Delta\lambda_B = 0, \Delta\lambda_D = 0.4$, red curve), and both décollement and bulk overpressures ($\Delta\lambda_B = \Delta\lambda_D = 0.4$, green curve). The blue (dry) and black (hydrostatic) curves initiate at the same α_c since $\tilde{\mathcal{P}}'_{ext}$ is proportional to $(\rho - \rho_f)$ (see first line in 18). The three curves have the same trend: the larger is $\tilde{C}_B$, the larger is the critical slope. The crossing between the blue and red curves at $\tilde{C}_B = 0.044$ and more generally the fact that the distance between the black and red curves is decreasing with increasing cohesion is more intriguing. This nonlinear trend is tentatively explained by considering the dimensionless overpressure in the décollement

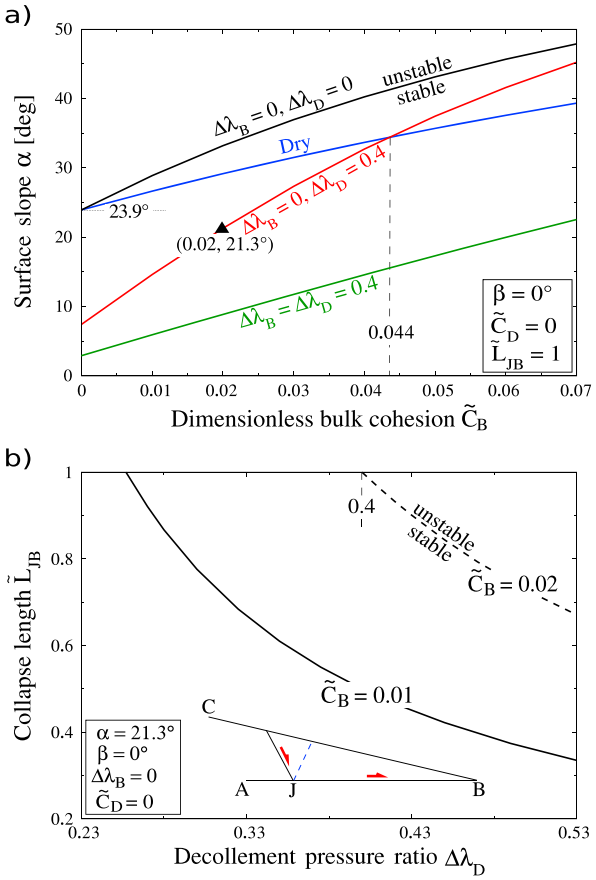

Figure 5. (a) The influence of the bulk cohesion $\tilde{C}_B$ on the critical slope α_c is presented where the value of α_c is computed at a series of values of bulk cohesion $\tilde{C}_B$ for the dry (blue curve), hydrostatic (black curve), and overpressure conditions on the décollement (red curve) and in the bulk (green curves), respectively. (b) The normalized collapse length $\tilde{L}_{JB}$ is shown as the function of the décollement fluid ratio $\Delta\lambda_D$ for bulk cohesion $\tilde{C}_B = 0.01$ and 0.02, respectively. The triangle in Figure 5a, bulk cohesion $\tilde{C}_B = 0.02$ (e.g., $C_B = 4.1$ MPa with an extent $L_{AB} = 10$ km), shows that the maximum slope of a stable wedge is less than 21.3°.

$\Delta\tilde{p} = -\Delta\lambda\rho g(x_2 + D)/C_B$ where x_2 is the second coordinate of a point in the décollement. Keeping this position constant while increasing C_B results in a decrease of the dimensionless pressure. This pressure term in the external power (18) thus decreases, and the results for no-overpressure (black curve) and with overpressure (red curve) should indeed converge for large values of the cohesion. Bulk overpressure, however, is very efficient at reducing α_c (green curve), and high-cohesion values are not sufficient to bring back α_c to the hydrostatic value.

The influence of the cohesion is also illustrated in Figure 5b where the length $\tilde{L}_{JB}$ is presented as a function of the fluid pressure ratio $\Delta\lambda_D$ for $\tilde{C}_B = 0.01$ and 0.02. For $\tilde{C}_B = 0.02$, the system is stable for $\Delta\lambda_D$ less than 0.4. For larger values the system is unstable for the largest slip extent $\tilde{L}_{JB} \simeq 1$. Note that shorter lengths are also unstable for $\Delta\lambda_D > 0.4$. However, the largest length remains the most unstable in the sense defined above that the difference $\tilde{\mathcal{P}}'_{mr} - \tilde{\mathcal{P}}'_{ext}$ is the largest. Decreasing the cohesion ($\tilde{C}_B = 0.01$) reduces the domain of stability in this fluid pressure ratio-length plane but does not alter the selection of the longest possible length at the onset of collapse.

3.4. Experimental Validation

The theory presented above indicates that the first collapse is associated with the maximum length of the décollement ($L_{JB} \simeq L_{AB}$). To provide an experimental validation of this claim, we propose to vary the angle β keeping a constant taper angle $\alpha + \beta$ in a laboratory experiment. This variation is conducted up to first failure to be able to inspect the first collapse mode.

The experimental setup consists of a rectangular glass box, initially horizontal, in which a wedge of cohesive material is built with a length $L_{AB} = 30$ cm and a maximum height 5 cm, yielding a taper angle of 9.5°, Figures 6a and 6b. It rests on a 2 mm thick glass microbeads layer. At the back, the wedge has a topography parallel to the décollement composed of a sandpaper. The experiment consists in lifting the back side of the box to increase the basal slope $\bar{\beta}$ until the wedge collapses by sliding against the fixed base and lateral walls. The basal dip at failure is denoted $\bar{\beta}_c$. Its value depends in particular on the cohesion of the material of the wedge. In most experiments (results indicated with an open circle in Figure 7) the material was in direct contact with the vertical lateral walls of the box. To estimate the bias due to this lateral friction, several experiments were conducted inserting a layer of glass microbeads between the wall and the material (results indicated with a black circle in Figure 7).

The analogue material production, characterization and implementation were done as follows. The bulk, cohesive materials are mixtures of CV32 eolian quartz sand (maker: SIFRACO, Sand CV32, 250 μm median grain size) and plaster in various proportions (Table 2, first and second columns). These materials were sifted to fill the box and the surface was then scraped to obtain the desired wedge shape. During scraping, some

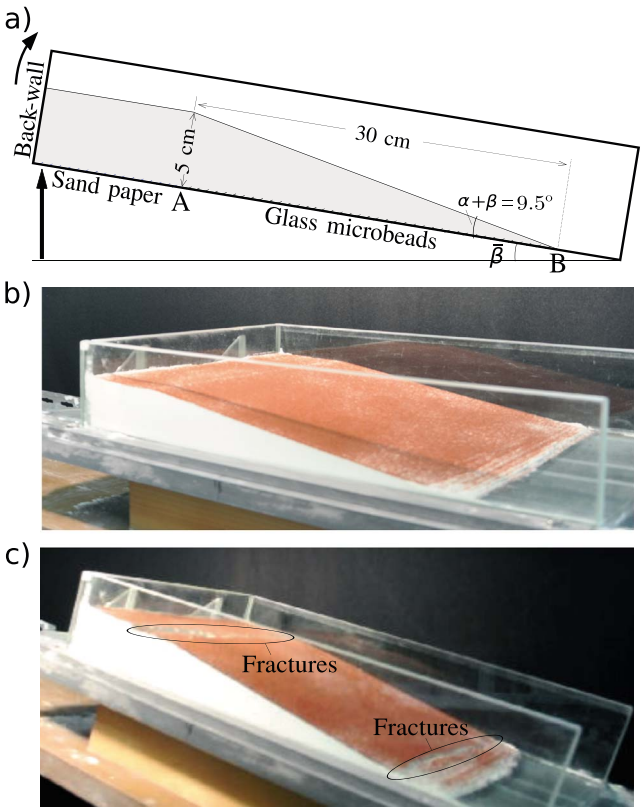

Figure 6. (a) Cross section of the experimental prototype proposed to check that the stability transition sees the maximum length of the décollement activated. (b) The photography presents the initial state. (c) The slope $\bar{\beta}$ is increased by lifting the back of the box (black arrows in Figure 6a) until the wedge collapses.

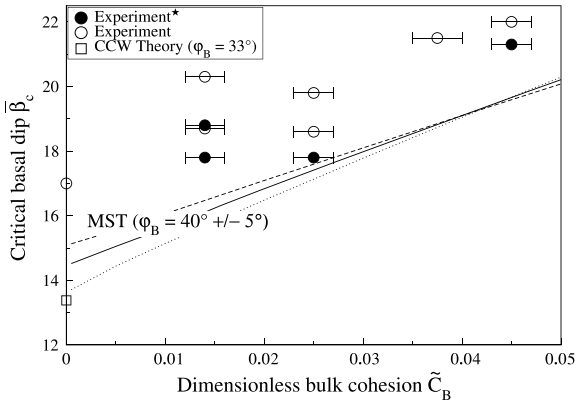

Figure 7. The critical basal dip $\bar{\beta}_c$ (taper angle constant, 9.5°) at the onset of gravitational collapse (Figure 6) as function of the cohesion of the wedge material. The open circle are experimental results with relatively high friction on the sidewall of the box, the black circle are obtained with lower lateral friction (glass microbeads between sidewall and bulk material, friction around 17 ± 1°). The dotted, solid, and dashed curve are the theoretical results of bulk friction angle φ_B = 35°, 40°, and 45°, respectively.

compaction of the pack is expected, thus perturbing its density and frictional properties. The use of triaxial tests or of a Casagrande box to measure the frictional properties of this class of analogue materials is precluded because the normal stress will compact the material and increase very substantially the cohesion beyond the value achieved in our setup. We nevertheless performed dedicated measurements of these properties. The density was measured using density cups [*Trautmann et al.*, 1985; *Maillot*, 2013], and the frictional properties (bulk cohesion C_B and friction angle φ_B) were estimated by digging a vertical cliff in the bulk material and increasing its height to its maximum value H_c until collapse. Collapse, at least theoretically, is associated with the sliding of a triangular section replacing the cliff by an inclined ramp. Such collapse mechanism has been considered recently for studying weathering of natural cliffs [*Utili and Crosta*, 2011] and is classical in the civil engineering literature [*Davis and Selvadurai*, 2005]. It is known that the material properties and the geometrical parameters of the collapse mechanisms are related by

$$H_c = \frac{4C_B}{\rho g}\frac{\cos(\varphi_B)}{1-\sin(\varphi_B)}, \quad \kappa = \pi/4 + \frac{\varphi_B}{2}, \tag{20}$$

with the ramp dip κ being the classical fault dip in extension for a Coulomb material. Results with the associated error range are shown in Table 2.

The décollement is composed of glass microbeads, a material of different frictional properties than the bulk. Cohesion is disregarded ($C_D = 0$), and the friction angle with glass is estimated by measuring the inclination required to initiate gravitational sliding of a thin-walled cylinder containing glass beads and resting on the glass base of the box. The basal friction is estimated to be $\varphi_D = 17 \pm 1°$.

Experimental and theoretical results are presented in Figure 6c, 7, and Table 2 (last two columns). The first observation (Figure 6c) is that the collapse involves the activation of the whole

Table 2. Parameters for Gravitational Collapse Experiments and for the Experiments Proposed to Estimate the Frictional and Cohesive Properties of the Sand and Plaster Mixture[a]

Material		Cliff Height	Slope Dip	Cohesion	Friction Angle	Density	Normalized Cohesion	Dip Measured
Sand	Plaster(wt %)	H_c (cm)	κ (deg)	C_B (Pa)	φ_B (deg)	ρ (g/cm^3)	$\tilde{C}_B$ (= $C_B/\rho g L_{AB}$)	$\bar{\beta}_c$ (deg)
100	0	-	-	0	30–33	1.710	0	17
85	15	3–4	62–68	50–70	35–45	1.515	0.012–0.016	18.7, 20.3, 18.8[b], 17.8[b]
75	25	6–7	62–68	100–120	35–45	1.464	0.023–0.027	18.6, 19.8, 17.8[b]
50	50	11–12	62–68	180–200	35–45	1.163	0.043–0.047	22, 22, 21.3[b]
25	75	9–10	62–68	150–170	35–45	0.931	0.035–0.040	21.5

[a]Note that the cohesion is not a monotonically increasing function of the plaster proportion.
[b]Values obtained in tests where glass microbeads were introduced along the sidewalls to reduce the friction.

length L_{AB} of the weak décollement. The frontal deformation observed at the tip of the wedge (Figure 6c) is due to imperfections of the surface slope toward the tip which are ignored in the present analysis.

The second observation is that $\bar{\beta}_c$ fluctuates by 1 or 2° when repeating experiments. Therefore, its increase with cohesion from an average of 17° to 22° is meaningful. It is in good agreement with the 5° increase predicted with the MST for three values of φ_B (35°, 40°, and 45°). However, the value of $\bar{\beta}_c$ for the experiments with lateral friction (open circles) is systematically larger by 2° or 3°, than predicted, either with the MST or the CCW theory ($\varphi_B = 33°$, the square in Figure 7) for cohesionless materials. We attribute this difference to spurious friction on the lateral walls. Indeed, experiments with reduced lateral friction (black circles) present a lower discrepancy, while keeping the same trend in the variation of $\bar{\beta}_c$ with $\tilde{C}_B$. According to *Souloumiac et al.* [2012], bias due to lateral friction depends on lateral to basal surface ratio of the material in contact with the glass box. Here this ratio is $5/28 = 0.18$, a value where lateral friction effects are small, but not negligible. If one could conduct experiments without lateral friction effects, the fit would be improved.

The main conclusions of that series of 10 experiments is that the collapse onset occurs for the largest possible slip extent and that the critical wedge angle is well predicted by the MST accounting for cohesion. The experimental uncertainties are coming mainly from the difficulty in (i) constructing homogeneous and reproducible packs and (ii) estimating the frictional properties of these packs at very low stress levels. In that respect, *Galland et al.* [2006] and *van Gent et al.* [2010] have proposed useful devices and protocols to characterize the friction, the cohesion, and the tensile strength, accounting for the initial compaction (or void ratio) of the powder.

4. Tectonic Extensional Collapse

The tectonic extensional collapse induced by the retreat of the vertical back wall is now discussed, Figure 1b. The upper bound to the force Q_u is calculated for the three different collapse mechanisms presented in Figure 8. The first mechanism is typical of a supercritical wedge sliding on its décollement as a rigid block. The second mechanism concerns a subcritical wedge, and the internal deformation is close to the back wall. The third mechanism is valid for both subcritical and supercritical wedges depending on the length L_{AG} of the activated décollement, measured from the back wall to the root (point *G*) of the normal fault (*GE*) and shear plane (*GF*). The two regions, BL and HG, have uniform velocities. The three mechanisms share the same velocity of the back wall $\underline{\hat{U}}_{BW}$, which is directed horizontally and of norm $\hat{U}_{BW}$ set to one. Note that for the three cases, slip between the bulk material and the back wall is accounted for. The derivation of the bounds is presented in the supporting information, and only the final results are provided here.

4.1. Mechanism (1): Décollement Fully Activated

The first collapse mechanism corresponds to the rigid translation of the wedge on the fully activated décollement at the uniform velocity of norm $\hat{U}_D$, a vector oriented by the angle φ_D from the décollement, see Figure 8a. The velocity jump at the back wall is the difference $\underline{\hat{U}}_{BW} - \underline{\hat{U}}_D$, a vector of norm $\hat{J}_{BW}$ and

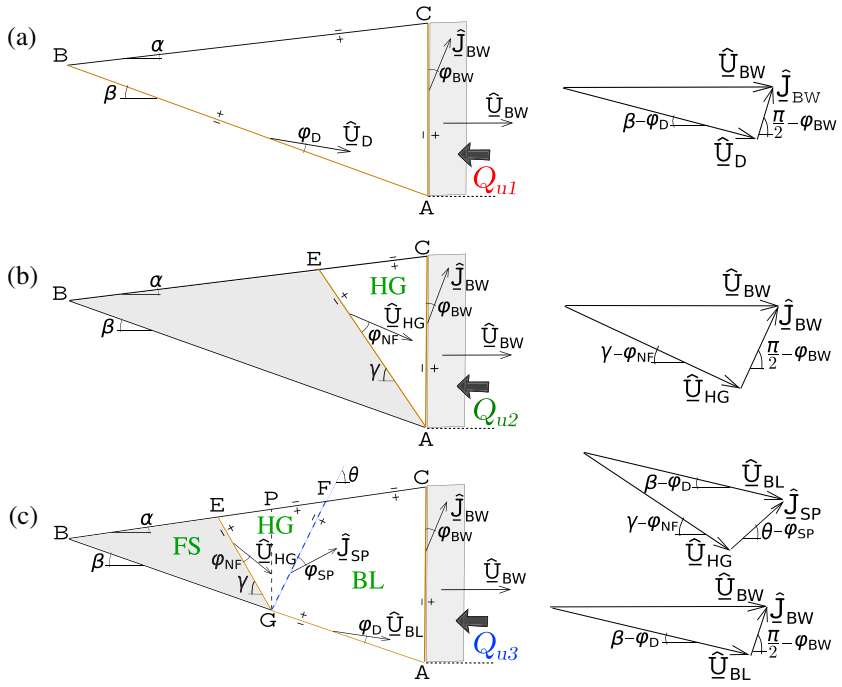

Figure 8. The tectonic extensional collapse is examined with three mechanisms corresponding to (a) the full activation of the décollement, (b) the activation of a normal fault (*AE*) rooting at the back wall, and (c) the partial activation of the décollement, of a normal fault (*GE*) and of a shear plane (*GF*). The hodograph of the velocities is also presented for each mechanism.

oriented by the angle φ_{BW} from the vertical direction. The application of the MST provides the tectonic upper bound Q_{u1}

$$Q_{u1} = C_D L_{AB}\cos(\varphi_D)\hat{U}_D + C_{BW}L_{AC}\cos(\varphi_{BW})\hat{J}_{BW} - (\rho-\rho_f)gS_{ABC}\hat{U}_D\sin(\beta-\varphi_D) - \Delta\lambda_D\rho g S_{ABC}\hat{U}_D\frac{\sin(\varphi_D)}{\cos\beta} + \frac{1}{2}\Delta\lambda_B\rho g L_{AC}^2\hat{U}_D\cos(\beta-\varphi_D) - \frac{p(A)+p(C)}{2}L_{AC}, \quad (21)$$

where C_{BW}, C_D, and S_{ABC} are the back-wall interface cohesion, the décollement cohesion, and the wedge area, respectively. Pressure at any point M is denoted by $p(M)$. The wedge velocity and the back-wall jump are related by

$$\hat{U}_D = \frac{\cos(\varphi_{BW})}{\cos(\varphi_{BW}-\beta+\varphi_D)}, \quad \hat{J}_{BW} = \frac{\sin(\beta-\varphi_D)}{\cos(\varphi_{BW}-\beta+\varphi_D)}, \quad (22)$$

according to the hodograph in Figure 8a.

4.2. Mechanism (2): A Normal Fault Rooting at the Back Wall

The second collapse mechanism consists of a normal fault rooting at the base of the back wall and dipping at γ, Figure 8b. There is no activation of the décollement. The half-graben has the uniform velocity field of norm $\hat{U}_{HG}$, which is oriented by the angle φ_{NF} from the normal fault, Figure 8b. The jump in velocity across the back-wall interface is $\underline{\hat{J}}_{BW} = \underline{\hat{U}}_{BW} - \underline{\hat{U}}_{HG}$ and is oriented with the angle φ_{BW} from back wall. The MST leads to the following expression for the tectonic upper bound Q_{u2}

$$Q_{u2} = C_{NF}L_{AE}\cos(\varphi_{NF})\hat{U}_{HG} + C_{BW}L_{AC}\cos(\varphi_{BW})\hat{J}_{BW} - (\rho-\rho_f)gS_{HG}\hat{U}_{HG}\sin(\gamma-\varphi_{NF}) - \Delta\lambda_B\rho g S_{HG}\hat{U}_{HG}\frac{\sin(\varphi_{NF})}{\cos\gamma} + \frac{1}{2}\Delta\lambda_B\rho g L_{AC}^2\hat{U}_{HG}\cos(\gamma-\varphi_{NF}) - \frac{p(A)+p(C)}{2}L_{AC}, \quad (23)$$

in which C_{NF} and S_{HG} are the normal fault cohesion and the surface of the half-graben. The velocities associated to this second collapse mechanism are

$$\hat{U}_{HG} = \frac{\cos(\varphi_{BW})}{\cos(\varphi_{BW}-\gamma+\varphi_{NF})}, \quad \hat{J}_{BW} = \frac{\sin(\gamma-\varphi_{NF})}{\cos(\varphi_{BW}-\gamma+\varphi_{NF})}, \quad (24)$$

are deduced from the hodograph in Figure 8b.

4.3. Mechanism (3): A Normal Fault and a Shear Plane Rooting on the Décollement

The third mechanism consists of the normal fault *GE* dipping at γ and the shear plane *GF* dipping at θ, Figure 8c. The two planes root at point *G* on the décollement which is activated from point *A* to *G*. The geometry of this third mechanism is thus described with three parameters: γ, θ and the distance L_{AG}. The velocities of BL and HG are uniform and denoted by $\underline{\hat{U}}_{\mathrm{BL}}$ and $\underline{\hat{U}}_{\mathrm{HG}}$. These velocities are oriented by the angles φ_D and φ_{NF} from the corresponding plane, see Figure 8c. There are two velocity discontinuities corresponding to the shear plane ($\underline{\hat{J}}_{\mathrm{SP}} = \underline{\hat{U}}_{\mathrm{BL}} - \underline{\hat{U}}_{\mathrm{HG}}$) and to the interface with the back wall ($\underline{\hat{J}}_{\mathrm{BW}} = \underline{\hat{U}}_{\mathrm{BW}} - \underline{\hat{U}}_{\mathrm{BL}}$). These two jumps are oriented by the angles φ_{SP} and φ_{BW} from the shear plane and to the back wall, respectively. The tectonic upper bound is

$$\begin{aligned} Q_{u3} = {} & C_{\mathrm{NF}} L_{GE} \cos(\varphi_{\mathrm{NF}}) \hat{U}_{\mathrm{HG}} + C_{\mathrm{SP}} L_{GF} \cos(\varphi_{\mathrm{SP}}) \hat{J}_{\mathrm{SP}} + C_D L_{AG} \cos(\varphi_D) \hat{U}_{\mathrm{BL}} \\ & + C_{\mathrm{BW}} L_{AC} \cos(\varphi_{\mathrm{BW}}) \hat{J}_{\mathrm{BW}} - (\rho - \rho_f) g S_{\mathrm{HG}} \hat{U}_{\mathrm{HG}} \sin(\gamma - \varphi_{\mathrm{NF}}) - (\rho - \rho_f) g S_{\mathrm{BL}} \hat{U}_{\mathrm{BL}} \sin(\beta - \varphi_D) \\ & - \Delta\lambda_D \rho g S_{AGPC} \hat{U}_{\mathrm{BL}} \frac{\sin(\varphi_D)}{\cos\beta} - \Delta\lambda_B \rho g S_{GEP} \hat{U}_{\mathrm{HG}} \frac{\sin(\varphi_{\mathrm{NF}})}{\cos\gamma} - \Delta\lambda_B \rho g S_{GFP} \hat{J}_{\mathrm{SP}} \frac{\sin(\varphi_{\mathrm{SP}})}{\cos\theta} \\ & + \frac{1}{2} \Delta\lambda_B \rho g L_{AC}^2 \hat{U}_{\mathrm{BL}} \cos(\beta - \varphi_D) - \frac{p(A) + p(C)}{2} L_{AC} \,. \end{aligned} \tag{25}$$

The velocity jumps over the shear plane and at the back wall are presented in two hodographs in Figure 8c. The application of the law of sines provides

$$\begin{aligned} & \hat{U}_{\mathrm{BL}} = \frac{\cos(\varphi_{\mathrm{BW}})}{\cos(\varphi_{\mathrm{BW}} - \beta + \varphi_D)} \,, \qquad \hat{J}_{\mathrm{BW}} = \frac{\sin(\beta - \varphi_D)}{\cos(\varphi_{\mathrm{BW}} - \beta + \varphi_D)} \,, \\ & \hat{J}_{\mathrm{SP}} = \hat{U}_{\mathrm{BL}} \frac{\sin(\varphi_D - \beta + \gamma - \varphi_{\mathrm{NF}})}{\sin(\theta - \varphi_{\mathrm{SP}} + \gamma - \varphi_{\mathrm{NF}})} \,, \quad \hat{U}_{\mathrm{HG}} = \hat{U}_{\mathrm{BL}} \frac{\sin(\theta - \varphi_{\mathrm{SP}} - \varphi_D + \beta)}{\sin(\theta - \varphi_{\mathrm{SP}} + \gamma - \varphi_{\mathrm{NF}})} \,. \end{aligned} \tag{26}$$

4.4. Comparison With CCW Theory for Extensional Collapse

The objective is to compare our predictions with the CCW theory for extensional collapse for dry, cohesionless materials [*Xiao et al.*, 1991]. These authors presented the CCW theory for extensional wedges and their results are illustrated in Figure 9a with the dotted, closed curve. Results are obtained for the material properties summarized in the fourth column of Table 1. The wedge is said to be supercritical within the region bounded by this curve: the whole décollement is activated. Outside this domain, we expect only the rear part of the décollement to be activated, next to the retreating wall.

It is proposed to compare the MST with the CCW theory in the following manner. Consider the two segments *AA*′ and *BB*′ in Figure 9a corresponding to a variation of the surface slope and the décollement dip, respectively. Along these segments, we compute the three upper bounds (21)–(26). The least of the three upper bounds is the closest to the exact, unknown tectonic force, and the corresponding mechanism is considered to be dominant.

Consider first the segment *AA*′ in Figure 9a along which $\beta = 32°$ and α varies within (−26°; 30°). The three upper bounds, normalized by $\rho g S_{ABC}$, along this transect are presented in Figure 9b. The collapse mechanism (1) (décollement fully activated) is dominant between point *A* and point A_{13} on the CCW stability curve (−14.7°). For larger values of α, it is mechanism (3) which is dominant up to point A_{23}. Mechanism (2) is dominant for the rest of the segment. These transitions from mechanism (1) to (3) and then (3) to (2) are illustrated in Figure 9c where the length of the activated décollement, normalized by L_{AB}, is presented. The value is 1 between *A* and A_{13}; it drops to a small value between A_{13} and A_{23} and finally drops to zero between A_{23} and *A*′. The MST has thus captured exactly the CCW predictions which is seen here as a transition between modes (1) and (3).

Consider now segment *BB*′ in Figure 9a along which $\alpha = 0°$ and β varies within (20°; 45°). From point *B* to B_{23}, it is mode (2) (no décollement activation) which is dominant. This last point marks the transition to mode (3) which dominates up to point B_{13} at the crossing of the CCW stability limit (36.7°). Within the supercritical domain, mode (1) dominates of course. The three upper bounds along this segment *BB*′ at the basis of this interpretation are presented in Figure 9d.

This method for probing the CCW stability boundary is repeated between points *C* and *C*′ to come to the conclusion that MST and CCW theories are in agreement.

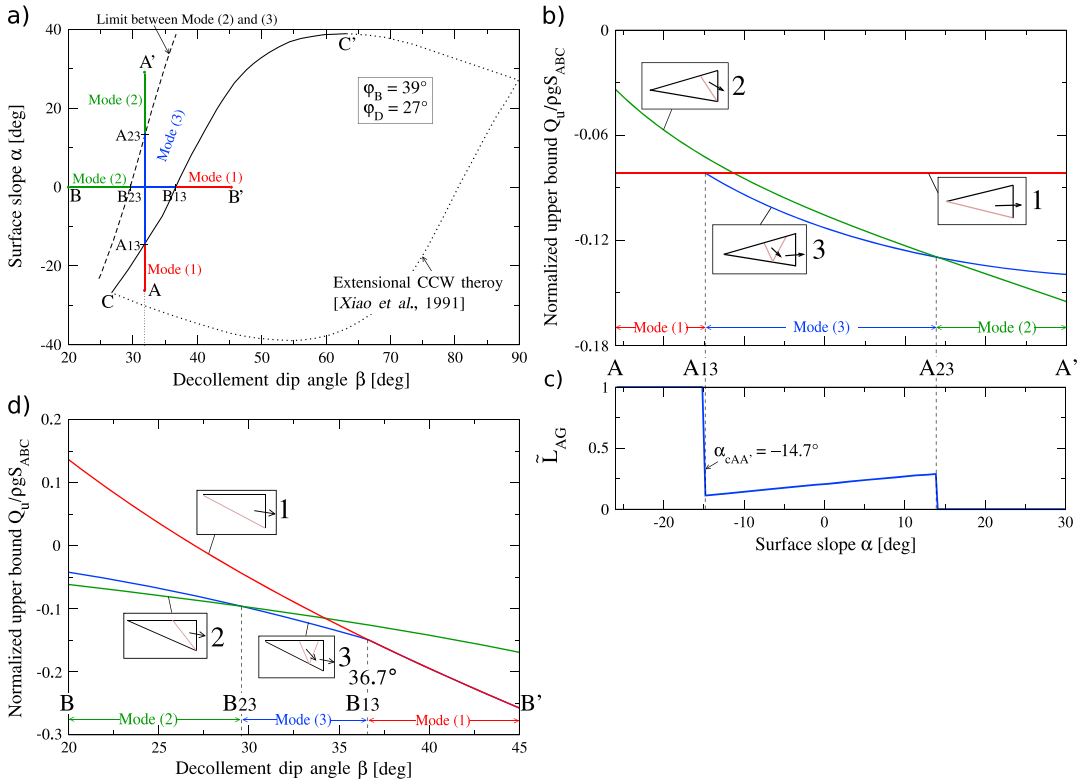

Figure 9. (a) The extensional CCW stability boundary [*Xiao et al.*, 1991] between points *C* and *C′* is shown to correspond to the transition between mode (1) (décollement fully activated) and mode (3) (partial activation). This finding is obtained by comparing the least upper bounds for the three modes along segment (b) *AA′* and (d) *BB′*. (c) The extent of the activated décollement along segment *AA′* is presented.

The new information is the role of the back wall, not accounted for in the CCW theory, which controls the collapse mechanism away from the stability boundary in the subcritical domain. The limit between mechanisms (2) and (3) as function of β is presented by the dashed curve in Figure 9a. This limit is dependent on the back-wall interface friction angle φ_{BW} (assumed equal to the bulk friction in this section). This finding is of course more relevant for the interpretation of experimental than field studies.

4.5. Experimental Validation

The concept of tectonic collapse mechanism is now validated by applying the MST to the interpretation of the sandbox experiment done by *Xiao et al.* [1991]. The sandbox is resting on an inclined ramp with a Mylar sheet acting as a décollement. The initial setup as well as the first mode of collapse are presented in Figure 10a. The left section of the sand body is sticking to the Mylar sheet while slip occurs along a short segment of the décollement close to the back wall. A normal fault roots at the left end of this segment and partitions the sand body into two regions, a graben being observed on the right of the box. Note from the inclined markers at the back wall the presence of a vertical zone of intense shear. The geometry of the sandbox ($\beta = 32°$, $\alpha = 0$), the sand friction angle ($\varphi_B = 39°$), and the friction on the décollement ($\varphi_D = 27°$) are provided by the authors. The missing information is the friction angle along the back wall.

The application of the MST is done in two steps. First, the nature of the first collapse mechanism is used to infer the frictional properties along the back wall. Second, the MST is applied on a modified topography to capture the jump in position of the collapse mechanism from the back-wall region to the left of the sandbox, Figure 11a.

To capture the missing material property, the three potential collapse mechanisms discussed in section 4 are considered. They do apply to this setup because the upward motion of the Mylar sheet is equivalent to the downward movement of the back wall. The first collapse mechanism corresponds to supercritical conditions. The second mechanism is subcritical and assumes that the slip occurs on the back wall and the onset of a normal fault rooting at its base. The dip of this fault is optimized. The third collapse mechanism

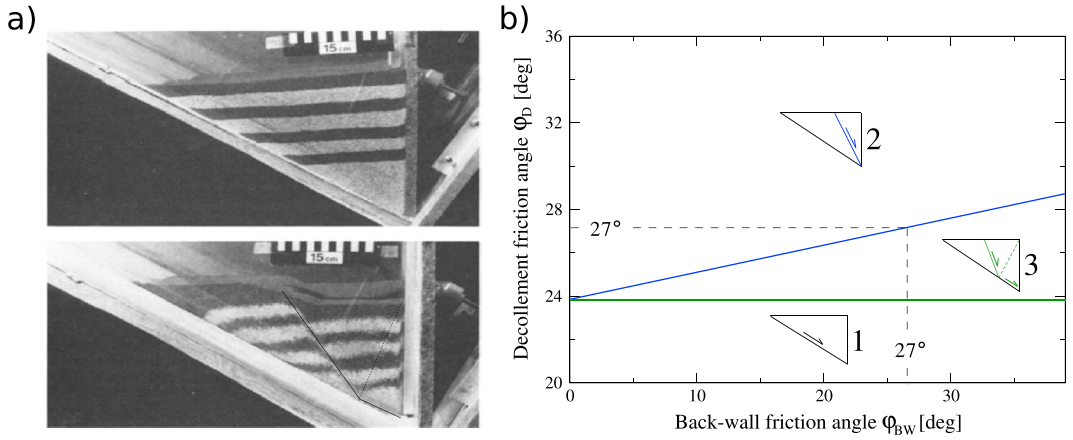

Figure 10. (a) Two photographs of the experiments of *Xiao et al.* [1991] showing the initial setup and the first collapse mechanism. (b) The map of dominant failure mechanism in the space spanned by the back wall and the décollement friction angles.

assumes that the lower part of the décollement is activated with a half-graben mechanism within the sand body. The dips of the two faults and the position of their common root on the décollement are found by optimization.

The dominance of these three mechanisms is now presented in a map spanned by the friction angle along the back wall (φ_{BW}) and the décollement friction angle (φ_D), Figure 10b. Material and interfaces are assumed cohesionless. It is seen that for a décollement friction angle below 23.8°, the whole décollement is activated, regardless of the back-wall friction. For larger décollement friction values, the dominance is divided between collapse mechanisms (2) and (3), the boundary between the two being the blue straight line in Figure 10b. Mechanism (2) with a normal fault rooting at the base of the retreating wall is dominant for the larger values of the décollement friction, and mechanism (3) is important in the intermediate range present in the triangular region of Figure 10b. Note that within this triangular domain, the shear plane conjugate to

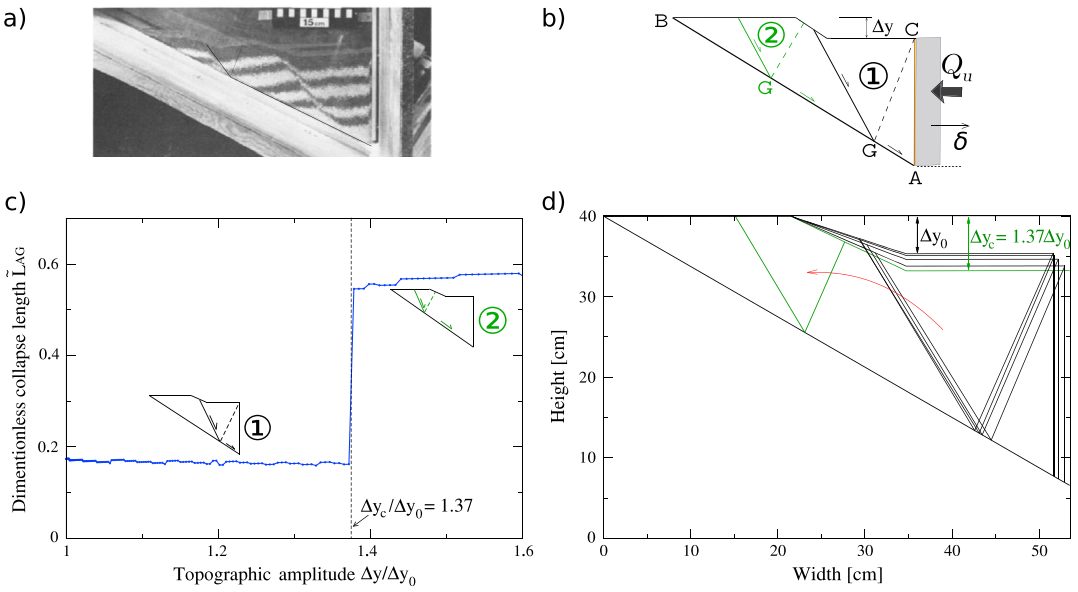

Figure 11. (a) The photograph taken from *Xiao et al.* [1991] shows the development of two collapse mechanisms, the first at the back-wall contact, and the second on the left of the sandbox. (b) The parametrization of the topographic evolution due to the development of the first collapse mechanism as well as the position of the second mechanism are illustrated. (c) The length of the activated décollement for the dominant mechanism as a function of the topographic step amplitude. (d) The idealized evolution of the geometry, the successive position of the frontal collapse mechanisms during topographic up to the transition to the second collapse mechanism (green).

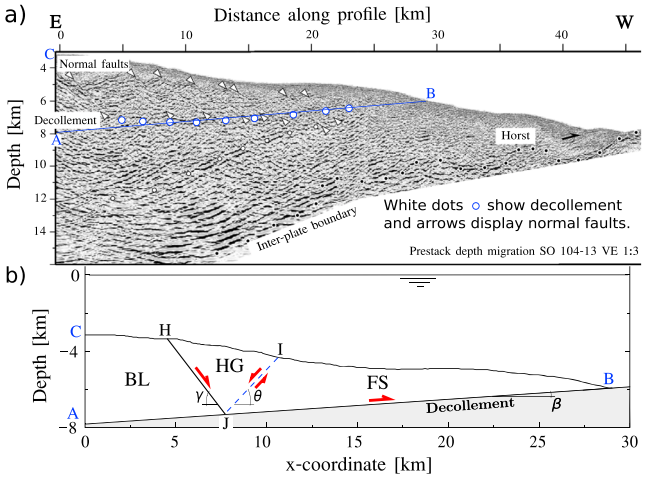

Figure 12. (a) Interpretation of the seismic section oriented east to west at the convergent margin off Antofagasta, North Chile, modified from *von Huene and Ranero* [2003] and *Sallarès and Ranero* [2005]. White dots show the detachment, and arrows display the normal faults existing in the wedge. (b) The optimized collapse mode is rooting in the region of overpressures idealized as a straight surface.

the normal fault is always outcropping at the top of the back wall. The first collapse noticed from the experiment of *Xiao et al.* [1991] is in this intermediate domain. The value $\varphi_D = 27°$ indicates further that the friction coefficient along the wall must thus be greater than 27°. The equality of these two friction angles is coincidental since there is no Mylar sheet between the back wall and the sand body. A friction angle φ_{BW} of 30° satisfy this condition for mechanism (3) to be dominant and is chosen for the sake of illustration in the rest of this analysis.

Our interpretation of the experimental findings of *Xiao et al.* [1991] is that collapse mechanisms (3) is activated and its development results in a step in the topography. This mechanism is nevertheless abandoned after a while for a new half-graben collapse more to the left, as seen in Figure 11a and illustrated in Figure 11b. It is proposed to capture this transition by modifying incrementally the geometry of our prototype and by repeating the application of the MST. For that purpose, the topography seen in Figure 10a prior to the transition of the collapse mechanism to the left is approximated by three segments. The segment to the left, unaltered by the deformation, being Δy above the segment to the right. The central segment has a linear slope between the two other horizontal segments. The vertical displacement Δy is starting from $\Delta y_0 = 4.6$ cm corresponding to the estimate made from the lower photograph in Figure 10a. The position of the retreating wall is computed by assuming that the area of sand seen through the glass wall is preserved during the experiment (a proxy for mass conservation).

The normalized collapse length $\tilde{L}_{AG}$ ($= L_{AG}/L_{AB}$) function of $\Delta y/\Delta y_0$ is shown in Figure 11c. The activity is occurring at the back of the wedge and four successive positions of the collapse mechanisms are presented in Figure 11d. The position of the root of the half-graben is displaced to the right following the wall displacement and the dips of the normal fault and shear plane seem to be unaltered. There is a critical $\Delta y_c = 1.37\,\Delta y_0$ at which the extent of the activated segment of the décollement changes drastically. The new collapse mechanisms (in green in Figure 11d) is then to the left. The new shear plane is outcropping within the transition zone of the topography. We shall not try to validate the value of Δy_c from the experimental results which may, incidentally, suffer from sidewall friction bias that would displace the new shear plane updip of the décollement [*Souloumiac et al.*, 2012]. Nevertheless, this exercise shows the versatility of the MST in capturing the essential features of the structural evolution. A dedicated experiment would certainly shed light on the qualitative merits of our predictions.

5. Application to North Chile

Having validated the collapse modes in extension, it is now proposed to apply the MST at the field scale accounting for potential overpressures, disregarded so far. The example of the North Chile margin in the area of the Mejillones peninsula [*Delouis et al.*, 1998] is proposed for that purpose. The subduction is taking place with erosion of the prism where the continental debris moved to the wedge toe are partly entering the subduction channel. This region has been recognized to be in extension above a weak detachment which is not the subduction interface but a subhorizontal fluid barrier within the continental plate [*von Huene and Ranero*, 2003; *Sallarès and Ranero*, 2005]. Normal faults are rooting in the detachment and participate to the extensive deformation resulting ultimately in erosion of the prism. Our objective is to determine the position of the active normal faulting, associated to our gravitational collapse mechanisms, as a function of the overpressure ratios within the detachment as well as in the bulk material.

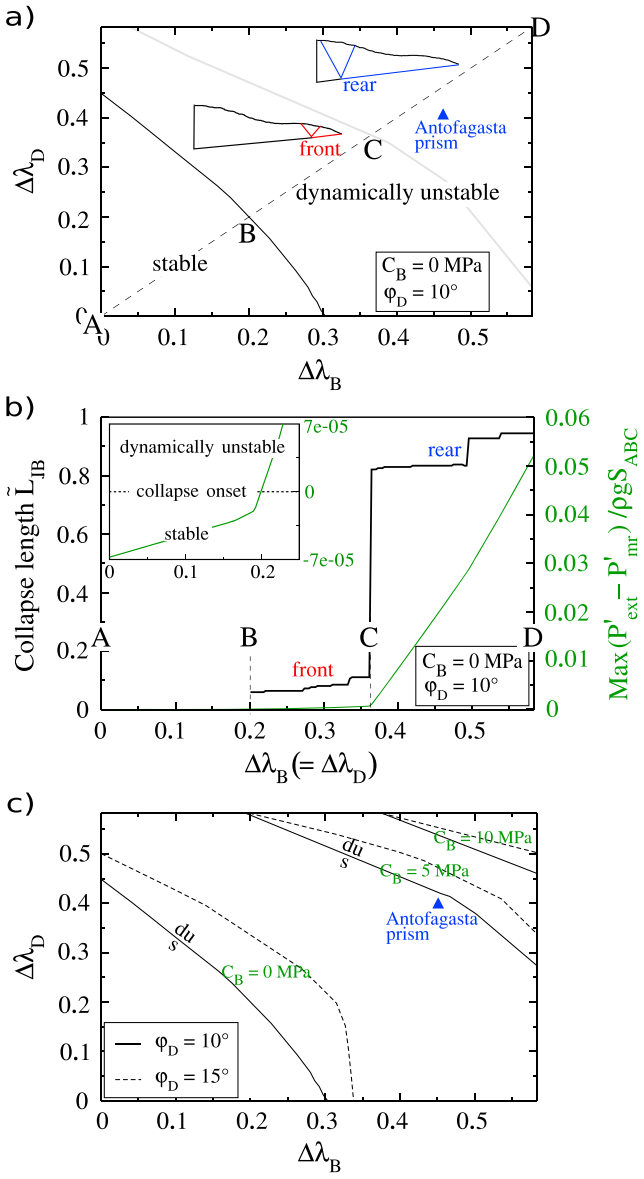

Figure 13. (a) The stability conditions map for the Antofagasta prism in the space spanned by the bulk and décollement overpressure ratios. (b) The position of the root of the dominant mechanism for equal pressure ratios and the lower bound to the acceleration power. (c) The sensitivity of the stability transition (s = stable; du = dynamically unstable) to the bulk cohesion and to the décollement friction angle.

The geometry of our prototype is constructed from the seismic section presented in Figure 9b of *Sallarès and Ranero* [2005] and shown here as Figure 12a from east to west. Of interest is the region above the interplate boundary which is approximated by the blue segment *AB* dipping at $\beta = 3.72°$ on average and of a total length of 29.1 km. It constitutes the décollement considered in all previous examples. The topography is discretized by a set of 236 points and the optimization of the gravitational collapse mechanism presented in Figure 12b consists in finding the maximum difference $\mathcal{P}'_{ext} - \mathcal{P}'_{mr}$ for all triplet (*H*, *I*, and *J*), as done in *Cubas et al.* [2008]. Note that the gravitational collapse activates the section *JB* of the décollement resulting in an upward motion of the frontal part of the wedge. The material property values or ranges are summarized in the fifth column of Table 1. The bulk friction angle φ_B is 27.9 ° (tan $\varphi_B = 0.51$ in *von Huene and Ranero* [2003]) and is equal to the friction angle of the normal fault and shear plane ($\varphi_{NF} = \varphi_{SP} = \varphi_B$). These equalities would be typical of faults at their onset prior to the development of any damage. The décollement friction angles is set to either 10° or 15°. The décollement cohesion is assumed to be zero and the bulk cohesion is set to 0, 5, or 10 MPa. The material and fluid volumetric masses are 2400 and 1030 kg/m^3, respectively [*Adam and Reuther*, 2000; *Sallarès and Ranero*, 2005].

Results are presented in Figure 13a in a plane spanned by the fluid overpressure ratios in the décollement and in the bulk material. Material and interfaces are assumed cohesionless. The resulting stability map has three regions. The first region, for low values of both pressure ratios, corresponds to stable conditions. The collapse mechanism cannot be activated. The second region is central within the stability map and is bounded on top by the grey curve. An instability mode occurs for these pressure conditions resulting in a gravitational collapse which is found at the front of the wedge. The third region corresponds to large values of the two pressure ratios. The mode of instability is then found more to the back of the structure.

von Huene and Ranero [2003] employed the CCW theory to study this erosional margin assuming the average friction coefficient and pore fluid pressure proposed by *Lallemand et al.* [1994]. We deduce from their data using the relation $\mu_D^\star = \mu_D(1 - \lambda_D)/(1 - \lambda_B) = 0.24$, assuming $\varphi_D = 10°$, that the pressure ratios are $\lambda_D = 0.837$ and $\lambda_{hydro} = \rho_f/\rho = 0.42$ in our analysis. Consequently, the pressure ratio differences should be

$\Delta\lambda_D = 0.41$ and $\Delta\lambda_B = 0.46$. These pressure conditions correspond to the blue triangle in our stability map in Figure 13a which is in the dynamically unstable domain with a dominant collapse at the back.

The position of the dominant collapse mechanism as well as the lower bound to the acceleration power provided by the maximum difference in $\mathcal{P}'_{\text{ext}} - \mathcal{P}'_{\text{mr}}$ are now discussed to illustrate the transition between the three stability regions defined above, Figure 13b. For the sake of simplicity, the horizontal axis corresponds to the diagonal *ABCD* in the pressure map of Figure 13a. The normalized length is defined between points *B* and *D* only since the segment *AB* is stable. The normalized, activated décollement length is small compared to one between *B* and *C* and large between *C* and *D*, the two main jumps corresponding to the stability transitions discussed above. The minor jumps between *B* and *C* and between *C* and *D* are controlled by the local accidents in the topography and are reminiscent of the findings of *Pons and Leroy* [2012]. More interesting is the variation in the lower bound to the acceleration power. This bound is negative between *A* and *B* (stable conditions) and increases approximately linearly between *C* and *D* independently of the jumps in position of the collapse mechanism. Consequently, it appears that the pressure conditions of *von Huene and Ranero* [2003] correspond to a dynamically unstable mode which is not sustainable. The pressure conditions and the material properties should be such that the blue triangle in Figure 13a is close to point *B* at the critical stability threshold.

To assess the role of the material properties in setting these stability predictions, it is now proposed to vary the bulk cohesion and the décollement friction angle, Figure 13c. The stability transitions are presented as solid and dashed curves for φ_D equal to 10° and 15°, respectively. Three sets of these two curves are presented corresponding to a cohesion of 0, 5, and 10 MPa. Increasing those two material properties reduces the domain of instability in that map. Furthermore, we observe that the set ($\varphi_D = 10°, C_B = 5$ MPa) leads to a stability transition close to the field conditions considered by *von Huene and Ranero* [2003].

6. Conclusion

This contribution proposes a mechanical analysis of two types of extensional deformations. First, gravitational collapse of a wedge of frictional material resting on a low friction inclined base (décollement), and second, tectonic collapse triggered by downdip slip on the décollement, following the retreat of the back wall. In the CCW theory the first case corresponds to compressive wedges at their maximum taper, i.e., on the verge of failure by instability of the topography, while the second case corresponds to extensional wedges, also at their maximum taper. The perfect match observed between the limit analysis and the CCW solutions, once properly amended, for various overpressures and friction angles completes the validation of our approach that was started in the classical compressive tectonic setting, without overpressures [*Cubas et al.*, 2008] and with overpressures [*Pons and Leroy*, 2012]. In all cases, the kinematic approach of limit analysis (referred to here as the maximum strength theorem or MST) generalizes the results of the CCW theory by including a wedge of finite size, limited by a back wall, and material with cohesion, thus providing a length scale in the solution. It also includes two important features for application to real experimental or natural cases: an arbitrary topography and preexisting faults as true discontinuities. The method remains, however, semianalytical, requiring only a discretization of the topography and moderate numerical implementation.

The study of the gravitational collapse for a triangular wedge of finite extent has lead to the conclusion that the maximum possible length of décollement is activated at the stability transition despite the introduction of a characteristic length in the problem via the material cohesion. The conclusion is not the same once the same gravitational mode is applied at the field scale for the North Chile margin considering the overpressured detachment studied by *von Huene and Ranero* [2003] and *Sallarès and Ranero* [2005]. The stability transition, if the bulk and décollement pressure ratios were equal and increased, is marked by a frontal collapse controlled by the specifics of the topography. It is only for large values of these pressure ratios, corresponding to dynamically unstable equilibrium states, that the collapse activates the maximum possible detachment length. These results obtained for zero cohesion indicates that the pressure conditions proposed by *von Huene and Ranero* [2003] would correspond to dynamic conditions. The introduction of bulk cohesion (order of 5 MPa) is found to be sufficient to reconcile our stability transition predictions with the proposed pressure conditions. The gravitational collapse is then frontal, consistent with the idea that erosion above the detachment is bringing material to the wedge toe.

The proposed methodology is now ready for use for field cases. It could be used, for example, to test the idea that the Tohoku-Oki earthquake corresponds indeed to a gravitational collapse of the wedge front updip the

décollement [*Cubas et al.*, 2013a]. The analysis could be semianalytical as proposed here or rely on numerical implementation of the MST [*OptumG2*, 2014] as proposed in *Cubas et al.* [2013b] to capture the activation of major splay faults in the Maule earthquake area. The advantage of the numerical approach is that a stress field can be obtained, either as a dual field to the velocity field for the MST or as a statically admissible field if the static approach of limit analysis is considered.

There are several potential extensions to the present work. The analysis of *Xiao et al.* [1991] with the tectonic collapse mode gave a glimpse at one of them. In this analysis, the geometry of the sand body was modified once the collapse mechanism was optimized based on simple rules close to the ones adopted by *Groshong* [1989]. After each geometry modification a new search for the collapse mechanism is conducted until a rear collapse is detected. This staggered scheme, optimization followed by geometrical evolution is at the basis of the sequential limit analysis considered for kink folds by *Maillot and Leroy* [2006] and *Kampfer and Leroy* [2009, 2012] and for accretionary wedges on the large scale by *Cubas et al.* [2008] for a single sequence of fault-related folds and by *Mary* [2012] and *Mary et al.* [2013a, 2013b] for an arbitrary number of sequences resulting in a large amount of shortening. It is clear that such evolution could also be constructed for extensional collapse. Furthermore, one could imagine to combine the frontal, compressional, and the rear extensional collapses to produce the deformation styles of many sedimentary basins as the Niger Delta [*Kostenko et al.*, 2008] while accounting for overpressures. The question of lateral compaction which can be important in such settings [*Butler and Paton*, 2010] will require not only to add a finite resistance to compression in the Coulomb criterion (as done by *Maillot and Leroy* [2006], for the hinge in kink folds) but also to keep memory of the compacted regions in the sequential limit analysis process, an opened technical question.

Some theoretical questions specific to gravitational collapse remain, however, to be clarified before proceeding. The present approach does not allow us to determine the power of acceleration, and therefore, we have no time scale to follow the evolution of a gravitational collapse. A proposition could be to use the lower bound to the acceleration powers and to use a classical Newmark's scheme following the geometry evolution which defines the displacement field. Any tentative algorithm will need to be compared to a full numerical solution for a sand body undertaking arbitrary large deformation and the recent developments of the particle finite-element method [*Zhang et al.*, 2013] is certainly a good candidate.

Appendix A: Different Fluid Pressure Parametrizations

The definition of the pressure ratio, introduced by *Hubbert and Rubey* [1959], requires a parametrization of the path from the free surface to the point of interest. Various authors have introduced their parametrizations leading to different definitions of the fluid pressure ratio. These differences are minor in compression because the taper angle remains small. However, in extension, this angle is sufficiently large to exacerbate these differences and the stability verdict becomes sensitive to the exact definition. The objective of this appendix is to compare the various parametrizations found in the literature.

The parametrization of *Hubbert and Rubey* [1959] for $\lambda^{(H)}$ (the first author name will be attached in superscript to the ratio) relies on a vertical path from the free surface to the point of interest. This path corresponds to the black line in Figure A1 and was used also by *Pons and Leroy* [2012] since it is the most natural parametrization for an irregular topography. *Davis et al.* [1983] and *Dahlen* [1984] used different parametrization corresponding to the red $\lambda^{(D1)}$ and blue path $\lambda^{(D2)}$, respectively, in Figure A1. The method to derive the relation between these different pressure ratios is that the pressure at any point P in the bulk should be uniquely defined.

The three definitions introduced so far and applied at the same point P are

$$\lambda^{(H)} = -\frac{p_f^{(H)} - \rho_f g D^{(H)}}{\sigma_z^{(H)} + \rho_f g D^{(H)}} \quad \text{with} \quad \sigma_z^{(H)} = -\rho g (z^{(H)} - D^{(H)}) - \rho_f g D^{(H)},$$

$$\lambda^{(D1)} = \frac{p_f^{(D1)} - \rho_f g D^{(D1)}}{\sigma_z^{(D1)} - \rho_f g D^{(D1)}} \quad \text{with} \quad \sigma_z^{(D1)} = \rho_f g D^{(D1)} + \rho g (H^{(D1)} - z^{(D1)}),$$

$$\lambda^{(D2)} = -\frac{p_f^{(D2)} - \rho_f g D^{(D2)}}{\sigma_z^{(D2)} + \rho_f g D^{(D2)}} \quad \text{with} \quad \sigma_z^{(D2)} = -\rho g z^{(D2)} \cos\alpha - \rho_f g D^{(D2)}, \tag{A1}$$

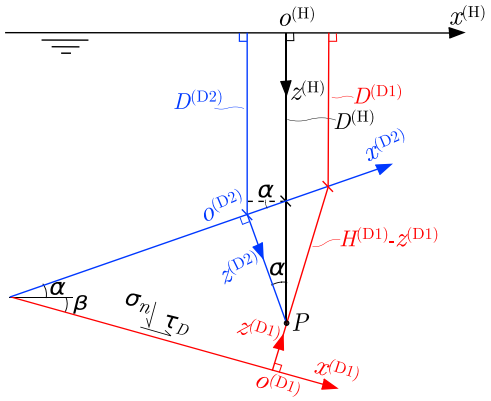

Figure A1. The definition of the fluid pressure ratio λ is sensitive to the path used from the free surface to the point of interest where the pressure is estimated. The black segment was proposed by *Hubbert and Rubey* [1959] and considered by *Pons and Leroy* [2012]. The red path was used by *Davis et al.* [1983], and the blue path was employed by *Dahlen* [1984]. The three different paths lead to the same fluid pressure at point *P* but to different pressure ratios.

complemented by the following geometric relations

$$\begin{aligned} D^{(D2)} - D^{(D1)} &= (H^{(D1)} - z^{(D1)}) \sin(\alpha+\beta) \sin\alpha\,, \\ D^{(D2)} - D^{(H)} &= (z^{(H)} - D^{(H)}) \sin^2\alpha\,, \\ z^{(D2)} &= (H^{(D1)} - z^{(D1)}) \cos(\alpha+\beta)\,, \\ z^{(D2)} &= (z^{(H)} - D^{(H)}) \cos\alpha\,. \end{aligned} \tag{A2}$$

The system of three equations in (A1) and (A2) has four unknowns, the pressure ratios and the actual pressure at point *P*: $p_f^{(H)} = p_f^{(D1)} = p_f^{(D2)}$. Eliminate the latter and obtain

$$\begin{aligned} \lambda^{(D1)} &= \lambda^{(D2)} \cos(\alpha+\beta)\cos\alpha + \frac{\rho_f}{\rho} \sin(\alpha+\beta)\sin\alpha\,, \\ \lambda^{(H)} &= \lambda^{(D2)} \cos^2\alpha + \frac{\rho_f}{\rho} \sin^2\alpha\,. \end{aligned} \tag{A3}$$

The trigonometric dependence is such that $\lambda^{(H)}$ and $\lambda^{(D2)}$ are rather different if the topographic slope α is large, as for the gravitational collapses of interest here.

Appendix B: Exact Critical Coulomb Wedge (ECCW) Theory

The classical CCW theory is now modified to account properly for the overpressure within the décollement. It complements the derivation found in *Wang et al.* [2006] and *Mourgues et al.* [2014], by providing the complete expression of the implicit solution in terms of the critical taper $\alpha + \beta$ as function of the fluid overpressures and friction angles. This expression is valid for any permissible value of the slopes α and β, thus the proposed name ECCW theory. We furthermore calculate and illustrate the solution in both gravitational and tectonic extensional cases. This ECCW theory is derived following exactly the steps of *Dahlen* [1984] and *Lehner* [1986] up to the condition of the décollement slip activation.

The tangential stress τ_D, Figure A1, to activate the décollement is given by

$$\tau_D = \tan(\varphi_D)(\sigma_n + p_D)\,, \tag{B1}$$

in which φ_D, σ_n, and p_D are the friction angle, the normal stress, and the fluid pressure in the décollement, respectively. The fluid pressure within the décollement is parametrized following Dahlen's choice as described in Appendix A:

$$p_D = -\lambda_D^{(D2)} \sigma_z + (1 - \lambda_D^{(D2)}) \rho_f g D^{(D2)}\,. \tag{B2}$$

The décollement tractions are now expressed in the (x, z) coordinate system also adopted in *Dahlen*'s [1984] (the blue coordinate in Figure A1)

$$\begin{aligned} \sigma_n &= \sigma_z - \tau_{xz} \sin 2(\alpha+\beta) - \frac{1}{2}(\sigma_z - \sigma_x)[1 - \cos 2(\alpha+\beta)]\,, \\ \tau_D &= \frac{1}{2}(\sigma_z - \sigma_x) \sin 2(\alpha+\beta) + \tau_{xz} \cos 2(\alpha+\beta)\,, \end{aligned} \tag{B3}$$

in terms of the stress components within the cohesionless wedge. This state of stress is on the verge of Coulomb failure and satisfies the local conditions

$$\begin{aligned} \frac{1}{2}(\sigma_z - \sigma_x) &= \frac{-\bar{\sigma}_z}{\csc(\varphi_B)\,\sec(2\Psi_O) - 1} \\ \tau_{xz} &= \frac{-\tan(2\Psi_O)\,\bar{\sigma}_z}{\csc(\varphi_B)\,\sec(2\Psi_O) - 1}\,, \end{aligned} \tag{B4}$$

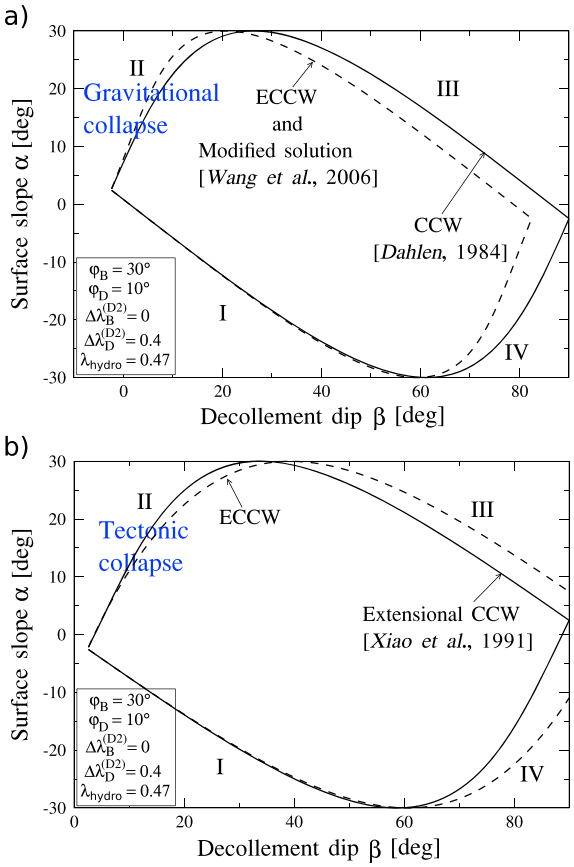

Figure B1. (a) Comparison of the ECCW theory and the solution of *Wang et al.* [2006] with the original theory of *Dahlen* [1984] for gravitational collapse. (b) Same comparison of the ECCW theory and the original extensional CCW theory of *Xiao et al.* [1991]. The bulk and décollement pressure ratios are defined in the Dahlen's fluid ratio $\lambda^{(D2)}$.

in which φ_B is the bulk friction angle, and the angle Ψ_O is measured between the maximum principal stress direction σ_1 and the x axis of the blue coordinate system (Figure A1). Also, the effective, vertical stress $\bar{\sigma}_z$ in (B4) is

$$\bar{\sigma}_z = \sigma_z + p_B = (1 - \lambda_B^{(D2)})(\sigma_z + \rho_f g D^{(D2)}). \tag{B5}$$

in which p_B and $\lambda_B^{(D2)}$ are the fluid pressure and the fluid pressure ratio in bulk material, respectively.

The set of five equations in (B1) to (B5) provides an implicit solution for the critical taper angle: $\alpha+\beta=\Psi_D-\Psi_O$ with

$$\Psi_D = \frac{1}{2}\arcsin\left[\left(\frac{1-\lambda_D^{(D2)}}{1-\lambda_B^{(D2)}}\right)\frac{\sin(\varphi_D)}{\sin(\varphi_B)} + \left(\frac{\lambda_D^{(D2)}-\lambda_B^{(D2)}}{1-\lambda_B^{(D2)}}\right)\sin(\varphi_D)\cos(2\Psi_O)\right] - \frac{1}{2}\varphi_D$$

$$\Psi_O = \frac{1}{2}\arcsin\left(\frac{\sin(\alpha')}{\sin(\varphi_B)}\right) - \frac{1}{2}\alpha'$$

$$\alpha' = \arctan\left[\left(\frac{1-\rho_f/\rho}{1-\lambda_B^{(D2)}}\right)\tan\alpha\right]. \tag{B6}$$

The quantity Ψ_D is the angle between σ_1 and the décollement, and this implicit definition is the only different term from the CCW theory, recalling the definition (13) and (19) in the contribution of *Dahlen* [1984]: $\Psi_D = \frac{1}{2}\arcsin\left[\frac{\sin(\varphi'_D)}{\sin(\varphi_B)}\right] - \frac{1}{2}\varphi'_D$ with $\varphi'_D = \arctan\left[\left(\frac{1-\lambda_D^{(D2)}}{1-\lambda_B^{(D2)}}\right)\tan(\varphi_D)\right]$. Obviously, the formulations of *Dahlen* [1984] is also the exact solutions if the bulk material, and décollement have the same fluid pressure ratio, $\lambda_D^{(D2)} = \lambda_B^{(D2)}$, or if they are both dry and subaerial.

The ECCW theory is now compared with the CCW theory using the coordinate definition considered by *Dahlen* [1984] in Figures B1a and B1b, corresponding to the gravitational collapse and the tectonic collapse modes, respectively. The material properties are summarized in the third column of Table 1. For overpressured décollement, the ECCW results do not differ significantly from the solutions of *Dahlen* [1984] and *Xiao et al.* [1991] in region I of Figures B1a and B1b. However, the differences are significant for region II (gravitational collapse or tectonic extension) of interest to this contribution. The critical slope α_c predicted from ECCW theory in region II, Figure B1a, is greater than the value of CCW theory. The ECCW theory produces a lower critical slope compared to the extensional CCW theory (region II in Figure B1b).

Acknowledgments
The first author is benefiting from the support of the China Scholarship Council during his doctoral studies in France. The authors thank David Boutelier (University of Newcastle, Australia) and the other anonymous reviewer for their comments to improve the final version of this manuscript. The codes used for the limit analysis calculations, to calculate the Exact CCW solutions, and the experimental data of Figure 7 are available at http://www.u-cergy.fr/fr/laboratoires/laboratoire-gec/equipement/logiciels.html.

References

Adam, J., and C. D. Reuther (2000), Crustal dynamics and active fault mechanics during subduction erosion: Application of frictional wedge analysis on to the north Chilean forearc, *Tectonophysics*, *321*, 297–325.

Butler, R. W. H., and D. A. Paton (2010), Evaluating lateral compaction in deepwater fold and thrust belts: How much are we missing from "nature's sandbox"?, *Geol. Soc. Am. Today*, *20*(3), 4–10.

Chen, W. F. (1975), *Limit Analysis and Soil Plasticity*, Elsevier, Amsterdam.

Cubas, N., Y. M. Leroy, and B. Maillot (2008), Prediction of thrusting sequences in accretionary wedges, *J. Geophys. Res.*, *113*, B12412, doi:10.1029/2008JB005717.

Cubas, N., J.-P. Avouac, Y. Leroy, and A. Pons (2013a), Low friction along the high slip patch of the 2011 Mw 9.0 Tohoku-Oki earthquake required from the wedge structure and extensional splay faults, *Geophys. Res. Lett.*, *40*, 4231–4237, doi:10.1002/grl.50682.

Cubas, N., J.-P. Avouac, P. Souloumiac, and Y. Leroy (2013b), Megathrust friction determined from mechanical analysis of the forearc in the Maule earthquake area, *Earth Planet. Sci. Lett.*, *381*, 92–103.
Dahlen, F. A. (1984), Noncohesive critical Coulomb wedges: An exact solution, *J. Geophys. Res.*, *89*(B12), 10,125–10,133.
Davis, D., J. Suppe, and F. A. Dahlen (1983), Mechanics of fold-and-thrust belts and accretionary wedges, *J. Geophys. Res.*, *88*(B2), 1153–1172.
Davis, R. O., and A. P. S. Selvadurai (2005), *Plasticity and Geomechanics*, Cambridge Univ. Press, Cambridge, U. K.
Delouis, B., H. Philip, L. Dorbath, and A. Cisternas (1998), Recent crustal deformation in the Antofagasta region (northern Chile) and the subduction process, *Geophys. J. Int.*, *132*, 302–338.
Galland, O., P. Cobbold, E. Hallot, J. d'Ars, and G. Delavaud (2006), Use of vegetable oil and silica powder for scale modelling of magmatic intrusion in a deforming brittle crust, *Earth Planet. Sci. Lett.*, *243*(3–4), 786–804.
Groshong, R. H. (1989), Half-graben structures: Balanced models of extensional fault-bend folds, *Geol. Soc. Am. Bull.*, *101*(1), 96–105.
Hubbert, M. K., and W. W. Rubey (1959), Role of fluid pressure in mechanics of overthrust faulting: I. Mechanics of fluid-filled solids and its application to overthrust faulting, *Bull. Geol. Soc. Am.*, *70*, 115–166.
Kampfer, G., and Y. Leroy (2009), Imperfection and burial-depth sensitivity of the initiation and development of kink-folds in laminated rocks, *J. Mech. Phys. Solids*, *57*, 1314–1339.
Kampfer, G., and Y. M. Leroy (2012), The competition between folding and faulting in the upper crust based on the maximum strength theorem, *Proc. R. Soc. A: Math. Phys. Eng. Sci.*, *468*(2141), 1280–1303.
Kostenko, O., S. Naruk, W. Hack, M. Poupon, H. Meyer, M. Mora-Glukstad, C. Anowai, and M. Mordi (2008), Structural evaluation of column-height controls at a toe-thrust discovery, deep-water Niger Delta, *Am. Assoc. Pet. Geol. Bull.*, *92*(12), 1615–1638.
Lacoste, A., B. C. Vendeville, R. Mourgues, L. Loncke, and M. Lebacq (2012), Gravitational instabilities triggered by fluid overpressure and downslope incision—Insights from analytical and analogue modelling, *J. Struct. Geol.*, *42*, 151–162.
Lallemand, S., P. Schnurle, and J. Malavieille (1994), Coulomb theory applied to accretionary and nonaccretionary wedges: Possible causes for tectonic erosion and/or frontal accretion, *J. Geophys. Res.*, *99*, 12,033–12,055.
Lehner, F. K. (1986), Noncohesive critical Coulomb wedges: An exact solution—Comments, *J. Geophys. Res.*, *91*(B1), 793–796.
Maillot, B. (2013), A sedimentation device to produce uniform sand packs, *Tectonophysics*, *593*, 85–94.
Maillot, B., and Y. M. Leroy (2006), Kink-fold onset and development based on the maximum strength theorem, *J. Mech. Phys. Solids*, *54*(10), 2030–2059.
Mandl, G., and W. Crans (1981), Gravitational gliding in deltas, in *Thrust and Nappe Tectonics*, edited by K. R. McClay and N. J. Price, *Geol. Soc. London Spec. Publ.*, *9*, 41–54.
Mary, B., B. Maillot, and Y. M. Leroy (2013a), Deterministic chaos in frictional wedges revealed by convergence analysis, *Int. J. Numer. Anal. Meth. Geomech.*, *37*, 3036–3051, doi:10.1002/nag.2177.
Mary, B., B. Maillot, and Y. M. Leroy (2013b), Predicting orogenic wedge styles as a function of analogue erosion law and material softening, *Geochem. Geophys. Geosyst.*, *14*, 4523–4543, doi:10.1002/ggge.20262.
Mary, B. C. L. (2012), Mécanique du prisme d'accrétion par l'approche cinématique de l'analyse limite et contributions expérimentales, Doctoral thesis, Université de Cergy-Pontoise, France.
Michalowski, R. (1995), Slope stability analysis: A kinematical approach, *Géotechnique*, *45*(2), 283–293.
Mourgues, R., and P. Cobbold (2003), Some tectonic consequences of fluid overpressures and seepage forces as demonstrated by sandbox modelling, *Tectonophysics*, *376*, 75–97.
Mourgues, R., E. Lecomte, B. Vendeville, and S. Raillard (2009), An experimental investigation of gravity-driven shale tectonics in progradational delta, *Tectonophysics*, *474*(3–4), 643–656.
Mourgues, R., A. Lacoste, and C. Garibaldi (2014), The Coulomb critical taper theory applied to gravitational instabilities, *J. Geophys. Res. Solid Earth*, *119*(1), 754–765, doi:10.1002/2013JB010359.
OptumG2 (2014), *Optum Computational Engineering*, Newcastle, Australia. [Available at www.optumce.com.]
Patton, T. L. (2005), Sandbox models of downward-steepening normal faults, *Am. Assoc. Pet. Geol. Bull.*, *89*(6), 781–797.
Pons, A., and Y. M. Leroy (2012), Stability of accretionary wedges based on the maximum strength theorem for fluid-saturated porous media, *J. Mech. Phys. Solids*, *60*, 643–664.
Salençon, J. (2002), *De l'élasto-Plasticité au Calcul à la Rupture, École Polytechnique*, Palaiseau, and Ellipses, Paris.
Sallarès, V., and C. R. Ranero (2005), Structure and tectonics of the erosional convergent margin off Antofagasta, north Chile (23°30'S), *J. Geophys. Res.*, *110,* B06101, doi:10.1029/2004JB003418.
Souloumiac, P., K. Krabbenhøft, Y. M. Leroy, and B. Maillot (2010), Failure in accretionary wedges with the maximum strength theorem: Numerical algorithm and 2D validation, *Comput. Geosci.*, *14*, 793–811, doi:10.1007/s10596-010-9184-4.
Souloumiac, P., B. Maillot, and Y. M. Leroy (2012), Bias due to side wall friction in sand box experiments, *J. Struct. Geol.*, *35*, 90–101.
Trautmann, C. H., F. Kulhawy, and T. D. O'Rourke (1985), Sand density measurements for laboratory studies, *Geotech. Test. J.*, *8*(4), 159–165.
Utili, S., and G. B. Crosta (2011), Modeling the evolution of natural cliffs subject to weathering: 1. Limit analysis approach, *J. Geophys. Res.*, *116*, F01016, doi:10.1029/2009JF001557.
van Gent, H. W., M. Holland, J. L. Urai, and R. Loosveld (2010), Evolution of fault zones in carbonates with mechanical stratigraphy—Insights from scale models using layered cohesive powder, *J. Struct. Geol.*, *9*, 1375–1391.
von Huene, R., and C. R. Ranero (2003), Subduction erosion and basal friction along the sediment-starved convergent margin off Antofagasta, Chile, *J. Geophys. Res.*, *108*(B2), 2079, doi:10.1029/2001JB001569.
Wang, K., J. He, and Y. Hu (2006), A note on pore fluid pressure ratios in the Coulomb wedge theory, *Geophys. Res. Lett.*, *33,* L19310, doi:10.1029/2006GL027233.
Withjack, M. O., Q. T. Islam, and P. R. Lapointe (1995), Normal faults and their hanging-wall deformation—An experimental study, *Am. Assoc. Pet. Geol. Bull.*, *79*(1), 1–18.
Xiao, H.-B., and J. Suppe (1992), Orgin of rollover, *Am. Assoc. Pet. Geol. Bull.*, *76*(4), 509–529.
Xiao, H.-B., F. A. Dahlen, and J. Suppe (1991), Mechanics of extensional wedges, *J. Geophys. Res.*, *96*(B6), 301–318.
Zhang, X., K. Krabbenhoft, D. M. Pedroso, A. V. Lyamin, D. Sheng, M. V. da Silva, and D. Wang (2013), Particle finite element analysis of large deformation and granular flow problems, *Comput. Geotech.*, *54*, 133–142.